J Neurophysiol 122: 1502–1517, 2019.
First published August 7, 2019; doi:10.1152/jn.00389.2019.

INNOVATIVE METHODOLOGY | *Control of Movement*

Behavioral training of marmosets and electrophysiological recording from the cerebellum

Ehsan Sedaghat-Nejad,[1] David J. Herzfeld,[1]* Paul Hage,[1]* Kaveh Karbasi,[1] Tara Palin,[1] Xiaoqin Wang,[2] and Reza Shadmehr[1]

[1]*Laboratory for Computational Motor Control, Department of Biomedical Engineering Johns Hopkins School of Medicine, Baltimore, Maryland; and* [2]*Laboratory for Auditory Neurophysiology Department of Biomedical Engineering Johns Hopkins School of Medicine, Baltimore, Maryland*

Submitted 26 June 2019; accepted in final form 1 August 2019

Sedaghat-Nejad E, Herzfeld DJ, Hage P, Karbasi K, Palin T, Wang X, Shadmehr R. Behavioral training of marmosets and electrophysiological recording from the cerebellum. *J Neurophysiol* 122: 1502–1517, 2019. First published August 7, 2019; doi:10.1152/jn.00389.2019.—The common marmoset (*Callithrix jacchus*) is a promising new model for study of neurophysiological basis of behavior in primates. Like other primates, it relies on saccadic eye movements to monitor and explore its environment. Previous reports have demonstrated some success in training marmosets to produce goal-directed actions in the laboratory. However, the number of trials per session has been relatively small, thus limiting the utility of marmosets as a model for behavioral and neurophysiological studies. In this article, we report the results of a series of new behavioral training and neurophysiological protocols aimed at increasing the number of trials per session while recording from the cerebellum. To improve the training efficacy, we designed a precisely calibrated food regulation regime that motivates the subjects to perform saccade tasks, resulting in ~1,000 reward-driven trials on a daily basis. We then developed a multichannel recording system that uses imaging to target a desired region of the cerebellum, allowing for simultaneous isolation of multiple Purkinje cells in the vermis. In this report, we describe *1*) the design and surgical implantation of a computer tomography (CT)-guided, subject-specific head post, *2*) the design of a CT- and MRI-guided alignment tool for trajectory guidance of electrodes mounted on an absolute encoder microdrive, *3*) development of a protocol for behavioral training of subjects, and *4*) simultaneous recordings from pairs of Purkinje cells during a saccade task.

NEW & NOTEWORTHY Marmosets present the opportunity to investigate genetically based neurological disease in primates, in particular, diseases that affect social behaviors, vocal communication, and eye movements. All of these behaviors depend on the integrity of the cerebellum. We present training methods that better motivate the subjects, allowing for improved performance, and we also present electrophysiological techniques that precisely target the subject's cerebellum, allowing for simultaneous isolation of multiple Purkinje cells.

cerebellum; marmoset; saccade; surgical methods; training methods

> In our parks, are there any trees more elegant and luxurious than the Purkinje cell from the cerebellum?
>
> Santiago Ramon y Cajal[1]

INTRODUCTION

The common marmoset (*Callithrix jacchus*) has gained attention for neurophysiological investigation in recent years because of its potential for transgenic manipulation (Kishi et al. 2014;Miller et al. 2016; Sasaki et al. 2009). Marmosets are small, New World primates with no known lethal zoonotic diseases that are transmittable to humans (Wakabayashi et al. 2018). Behaviorally, they share important attributes with us: they are social and live in family units, they are vocal and rely on species-specific sound production for their communication, and they are visual and use saccadic eye movements to explore their environment. Notably, for a primate they have a particularly short gestation period (~5 mo) and regularly give birth to twins or triplets. Thus they have a high breeding efficiency with potential for germline transmission of genetically modified models.

Indeed, marmoset research is benefiting from transgenic (Sasaki et al. 2009), gene-editing (Kishi et al. 2014), and optogenetic tools that target specific neurons (MacDougall et al. 2016). Thus marmosets have the potential to become a model system for investigating cognitive and social behaviors (Mustoe et al. 2015; Takahashi et al. 2017) and auditory (Wang 2018) and visual perception (Solomon and Rosa 2014), as well as neural control of vocalization (Eliades and Wang 2013; Eliades and Miller 2017; Roy et al. 2011) and eye movements (Johnston et al. 2018; Mitchell et al. 2014).

Many aspects of social behavior, vocalization, and eye movements depend on the integrity of the cerebellum. For example, children who suffer from autism spectrum disorder (ASD), a developmental disorder that leads to impairments in social and communication skills, exhibit anatomic abnormalities in their cerebellum, including a reduced number of Purkinje cells (Whitney et al. 2008), particularly along the vermis (Courchesne et al. 2001; Hashimoto et al. 1995; Murakami et al. 1989; Scott et al. 2009). Notably, in children with ASD, we found that damage to the cerebellum is prevalent in lobule VI

* D. J. Herzfeld and P. Hage contributed equally to this work.
Address for reprint requests and other correspondence: E. Sedaghat-Nejad, Traylor Building Room 416, Johns Hopkins School of Medicine, 720 Rutland Ave., Baltimore, MD 21205 (e-mail: e.sedaghatnejad@gmail.com).

[1] Cajal (1989), p. 364.

and parts of lobule VIII (Marko et al. 2015), regions that in the macaque are critical for control of saccadic eye movements (Barash et al. 1999; Takagi et al. 1998). Control of saccades in healthy subjects shows exquisite sensitivity to decision-related variables such as reward prediction error (Sedaghat-Nejad et al. 2019) and history of effort expenditure (Yoon et al. 2018). Thus marmosets may present a particularly good opportunity to investigate the role of the cerebellum in eye movements, social communication, and neurological diseases such as ASD.

However, despite these attractive features, there is concern that marmosets may be difficult to train for studies that investigate the neural basis of goal-directed behavior in a laboratory setting. This concern is due to the fact that in the current literature, the number of trials that these animals can perform within a session appears to be quite limited. For example, one recent study that trained marmosets to perform saccades found that, on average, they performed 80–100 trials per session (Johnston et al. 2018), whereas another study reported 300–800 trials per session (Mitchell et al. 2014).

These numbers are on the lower bound of what is needed to identify task-related neurons in the cerebellum. For example, identification of an eye-related Purkinje cell requires 200–300 trials to measure complex spike tuning and an additional 500–1,000 trials to measure the simple spike response to saccadic eye movements (Soetedjo and Fuchs 2006; Soetedjo et al. 2008). As a result, the relatively low numbers of trials per session reported earlier makes it unclear whether marmosets can serve as a model for neurophysiological studies of operant conditioned behavior.

Over the past 4 years, our team has been building a new marmoset laboratory, aiming to develop behavioral and neurophysiological protocols that allow for electrophysiological recording from the cerebellum of head-fixed animals. From a behavioral perspective, our goal was to ask whether the subjects could be motivated to produce a sufficiently large number of rewarded trials on a daily basis in the head-fixed configuration. From an electrophysiological perspective, our aim was to produce precise targeting of a region of the cerebellum, thus providing the means to simultaneously isolate multiple Purkinje cells using high-density electrodes.

To solve the training problem, we designed a carefully calibrated food regulation regime that motivated the subjects to perform a saccade task. To solve the electrophysiological problem, we developed a high-precision, acute multichannel recording system that resulted in simultaneous recording from multiple Purkinje cells within the cerebellar vermis.

In this report, we provide an account of our experience, in terms of both procedures that failed and those that succeeded, going from initial behavioral training through neurophysiological recording. We begin with the design of a computer tomography (CT)-guided subject-specific titanium printed head post, one that may be the first of its kind in the marmoset. We then describe the training and the MRI-guided electrode alignment procedures. We conclude with examples of simultaneously isolated pairs of Purkinje cells, a difficult accomplishment only once before reported in the awake behaving primate (Medina and Lisberger 2007).

METHODS

Subjects. The procedures were carried out on three marmosets: two female (*subject B*: 420 g, 11 yr old; *subject M*: 350 g, 4 yr old) and one male (*subject R*: 400 g, 4 yr old). All three subjects were born and raised in a colony that one of the authors (X. Wang) has maintained at the Johns Hopkins School of Medicine since 1996. The experimental procedures were evaluated and approved by Johns Hopkins University Animal Care and Use Committee in compliance with the guidelines of the US National Institutes of Health.

Design of head post and recording chamber. Recording from Purkinje cells of the cerebellum imposes particular demands on stability: one needs to not only isolate a neuron but also establish identity of that neuron via presence of both simple and complex spikes, which requires movable electrodes and longer periods of recordings. To stabilize the head during behavioral sessions, the current technique is to build an acrylic-based thick "helmet" atop the skull, which then serves as a base that holds two or more metal posts (Lu et al. 2001a). The glue-inserted metal posts are attached to bars that are fixed to a primate chair, thereby holding the head in a fixed position. A more recent method is a halo-like device that holds the skull inside a ring (Johnston et al. 2018). Both approaches have been used for recordings from the cerebral cortex. However, reaching the cerebellum requires open access to the posterior parts of the skull, making the halo approach less desirable. Furthermore, we aimed to produce an approach that reduced disruption of the underlying skin and muscles, resulting in a design that allowed for skin coverage of the skull and integrity of the temporalis muscles. This led us to develop a titanium-based head post and chamber design that eliminated use of the acrylic-based helmet and maximized the open area in the posterior part of the skull (Fig. 1).

To prepare for head fixation, we designed a head post based on the specific geometry of the surface of each subject's skull and manufactured it using three-dimensionally (3D) printed titanium. We began with a preoperative CT (Fig. 1*A*) and used it to build a 3D model of the skull (Fig. 1*B*). This was done using 3D Slicer, an open-source image analysis and visualization software (Fedorov et al. 2012). The 3D skull model was then imported into a computer-aided design (CAD) environment (SolidWorks and Autodesk Fusion 360), which informed the design of an X-shaped titanium head post (Fig. 1, *B* and *C*), a titanium base recording chamber (Fig. 1*D*), and a plastic protective chamber cap. The head post and base chamber designs were optimized to remain lightweight and within the anatomical constraints of the frontal eye ridge and the lateral ridges on the skull, allowing us to minimize damage to the temporalis muscle attachment. The head post and base chamber were 3D printed with laser-melted grade 5 titanium (6AI-4V; Sculpteo), producing a lightweight (3 g), biocompatible, corrosion-resistant structure. The protective cap that covered the chamber was 3D printed with polylactic acid (PLA) plastic filament (0.5 g).

Surgery. Implantation of the head post and chamber was conducted by a surgical team led by laboratory members and aided by veterinary technicians and veterinarians. The animal was anesthetized with alfaxalone (12 mg/kg), then intubated with a no. 2.0 uncuffed endotracheal (ET) tube, and administered isoflurane (1–1.25%, adjusted as needed) to maintain the anesthetic plane, as well as atropine and dexamethasone via intramuscular (IM) injections. The subject was then head-fixed by inserting bilateral ear bars into the osseous ear canal, which were fastened to a stereotaxic frame, and a bite bar was slid into place with a forehead clamp attachment to ensure that the head was positioned appropriately and securely with respect to the chest. Lidocaine (2%) and epinephrine (1:100,000) were then injected into the subcutaneous space beneath the scalp, and the operative region was treated with alternating cycles of diluted chlorhexidine and alcohol and at the very end sprayed with betadine. Next, we used a surgical marker to draw an outline for a midline incision on the scalp, extending 2 mm posterior to the supraorbital fat pad and extending to the occipital ridge. We then made the incision using a scalpel, and the skin was separated from the underlying fascia as well as the fascia from the underlying muscle. From here, the surface of the skull was prepared by removing residual tissue using curettes and 3% hydrogen

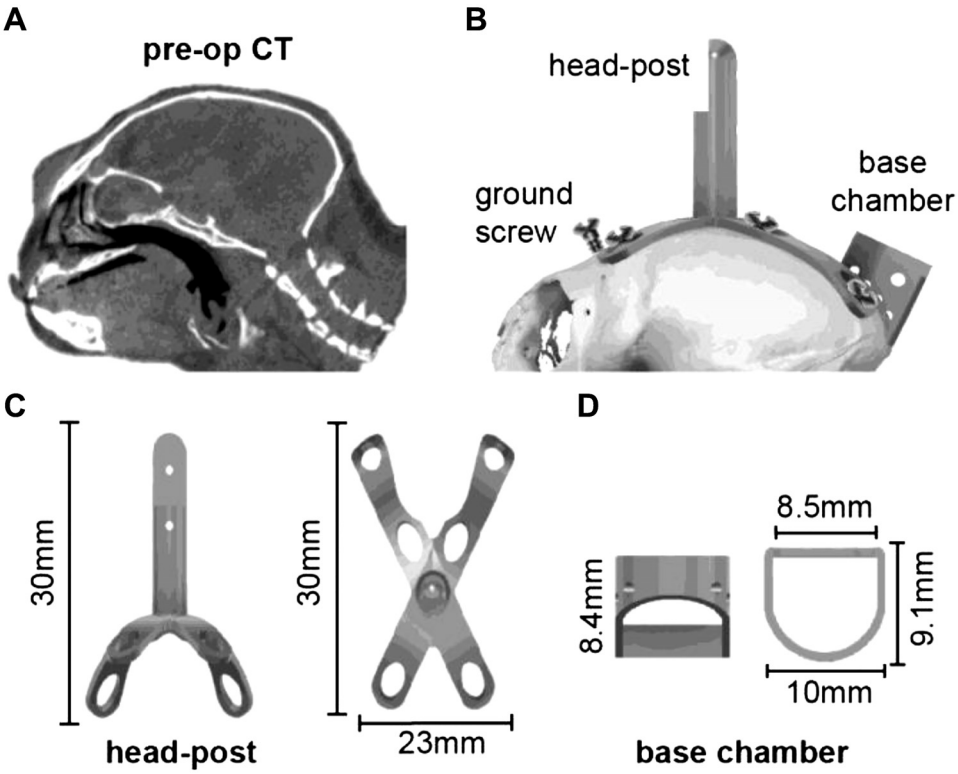

Fig. 1. Design of the head post and base chamber. *A*: preoperative computer tomography (pre-op CT) image that we used to build a geometric model of the surface of the skull. *B*: model of the head post and chamber fitted to the CT-based model of the animal's skull. The screws, head post, and chamber are titanium. *C*: head post (2.39 g), designed to precisely fit the curved geometry of the subject. *D*: base chamber (0.48 g).

peroxide solution, and the head post was positioned for implantation. The temporalis muscle was pushed backed from its bony insertions on the spots that intersected with the head post.

To attach the head post, phosphoric acid etchant was applied for 15–20 s and then rinsed. Next, a thin layer of OptiBond Solo Plus (Kerr) was applied to the surface of the skull, covering the entire area to be occupied by the head post, cranial ground screw, and base chamber. OptiBond Solo Plus was also applied to head post X-shaped legs and the lower half of the base chamber. After application, the OptiBond was cured using a UV gun. The screw locations were then marked and drilled using a #54 drill bit (1.4-mm diameter), with a stopper limiting the hole depth to 1.1 mm. NX3 dual-cure dental cement (Kerr.) was applied to the center of the bottom of the head post, placed on the skull, and then cured using UV light.

Titanium screws (self tapping, 2.0 × 4 mm, 0.04 g, or 2.0 × 5 mm, 0.05 g) were then used to affix the legs of the head post onto the skull. A cranial ground screw (titanium, self tapping 2.0 × 8 mm, 0.08 g) was screwed into the prepared hole (Fig. 1*B*). We confirmed that screw depth into the skull did not exceed 1.1 mm. Next, NX3 cement was applied inside head post screw holes and around the ground screw to ensure structural integrity of the implanted screws.

NX3 cement was also applied to the bottom edge of the base chamber, and the base chamber was placed between the rear legs of the head post (Fig. 1*B*) so that it was approximately located above the visual cortex and directed straight down. NX3 cement underwent a UV light curing. A final layer of NX3 cement was applied over the whole structure and was smoothed using Parafilm tape and then cured with UV light.

The total weight of the NX3 cement, the installed apparatus, and the screws was less than 8.5 g. With the implantation complete, the temporalis muscle and fascia were replaced to their original positions. Finally, the two skin flaps were reattached together via sutures using a 0/4 single-filament thread. As a result, the surgical procedure produced an animal in which the skin covered almost the entire skull, except for small regions dedicated to the frontal ground screw, the main bar of the head post, and the base chamber.

At this point anesthesia was discontinued and the ET tube removed. The animal was monitored as consciousness and motor function were regained. A second dose of dexamethasone (0.25 mg/kg) was administered via IM injection 12 h after the first dose. Recovery was monitored with daily postoperative checkups for 13 days, including inspection of the surgery site for infection, checking for integrity of the sutures, recording of vital signs, feeding, and the administering of drugs.

Establishing a chamber-based coordinate system for the cerebellum. Because of the small size of the skull and our chamber design, we found it difficult to attach a micromanipulator to the head post. Given that the micromanipulator was external to the head post, we were concerned that we might not be able to accurately target and reproducibly approach a desired location in the cerebellum. This led us to design an electrode guide system that we integrated into the chamber design (Figs. 2 and 3). Our problem was that during surgery, the base chamber was placed by hand on the skull, and therefore its location with respect to the cerebellum was unknown. Furthermore, postsurgical CT or MRI imaging of the implanted animal was possible but problematic because the titanium pieces generated substantial artifacts, making it difficult to precisely localize the base chamber.

To solve this problem, we designed a CT-visible reference ruler (Fig. 2) that we inserted into the base chamber. The reference ruler consisted of seven layers of a 1.5-mm marked grid system, 3D printed with PLA plastic filament (Fig. 2*B*). With the reference ruler inserted into the chamber, we performed a postoperative CT scan (Fig. 2*C*). This produced a clear image of the ruler, but with artifacts from the titanium. We then coregistered the preoperative CT (Fig. 1*A*) and the postoperative CT (Fig. 2*C*) using bony areas and coregistered the preoperative CT (Fig. 1*A*) and the preoperative MRI (Fig. 2*A*). Fixing preoperative CT between two registrations produced a coregistered image of all three images. The result was a full representation of the subject's head, including the reference ruler, the skull, and the brain (Fig. 2*D*).

We used the ruler, chamber, and skull geometry to plan electrode trajectories to arrive at 20 distinct points of interest in the cerebellum.

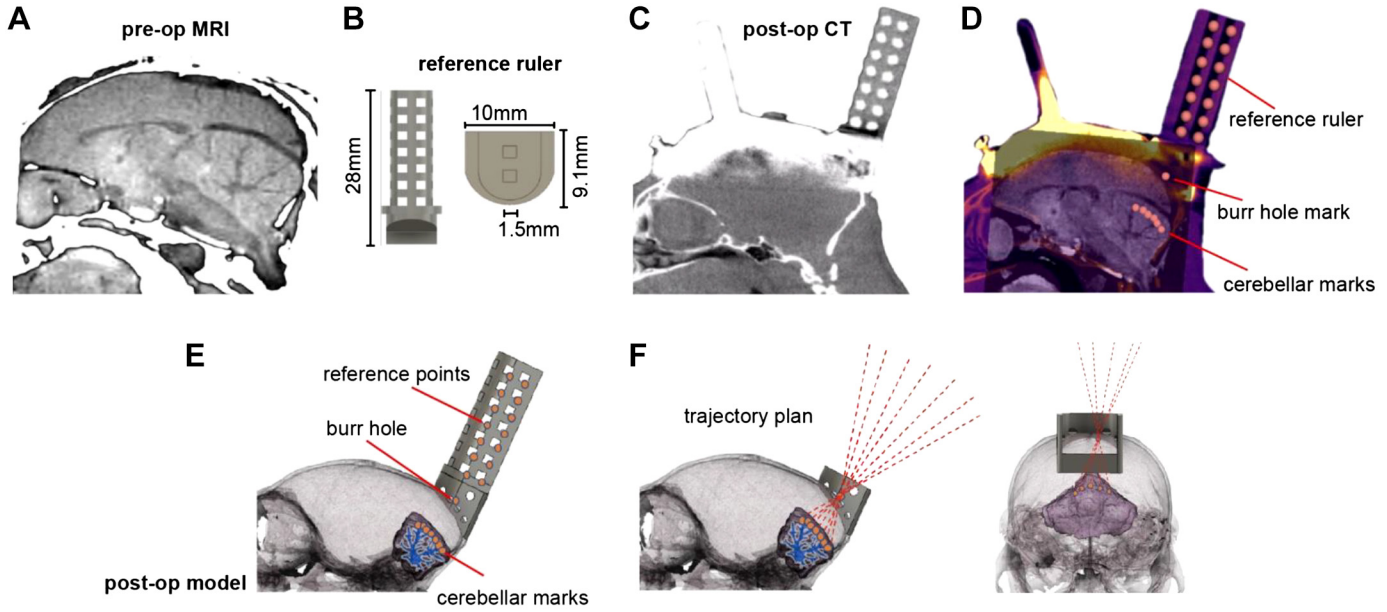

Fig. 2. Development of a chamber-based geometric model to define electrode trajectories and specify location of the burr hole. *A*: preoperative (pre-op) MRI image used for identifying the desired regions of interest in the cerebellum. *B*: reference axis ruler (1.104 g) that was inserted into the base chamber before postoperative computer tomography (post-op CT) imaging. *C*: post-op CT image after surgical installation of the head post, base chamber, and reference ruler. Although the reference ruler is clearly visible, the titanium head post and chamber have produced significant artifacts. *D*: coregistered pre-op CT, post-op CT, and pre-op MRI. Markers identify points on the reference axis and points in the cerebellum. A mark identifies the burr hole location. *E*: a 3-dimensional (3D) model that has coregistered the skull, cerebellum, chamber, and reference ruler. *F*: using the 3D model, we drew trajectories that began at points of interest in the cerebellum, converged on a single 1.5-mm-diameter burr hole on the skull, and then diverged beyond the chamber as cylinders within the guidance tool. These trajectories represented desired electrode paths.

In this design, all 20 trajectories traveled through a single 1.5-mm-diameter burr hole. To calculate each trajectory, we placed 21 points at various positions on the reference ruler (Fig. 2*D*), 1 point on the surface of the skull for a craniotomy burr hole (Fig. 2*D*), and 20 points at various locations along lobules V, VI, and VII of the vermis (Fig. 2*D*, "cerebellar marks"). The point representing the burr hole was placed at 1.1 mm lateral to the midline to avoid the superior sagittal sinus.

The various points were then imported into a CAD environment, along with a model of the brain that we generated with 3D Slicer from the MRI images (Fig. 2*E*). We aligned the imported points to their respective targets, guided by the coregistered image. The process relied on the alignment of all reference axis ruler points from the coregistered image (Fig. 2*D*) to the reference ruler within the model environment (Fig. 2*E*). This automatically aligned the burr hole and points on the cerebellum to the skull and brain

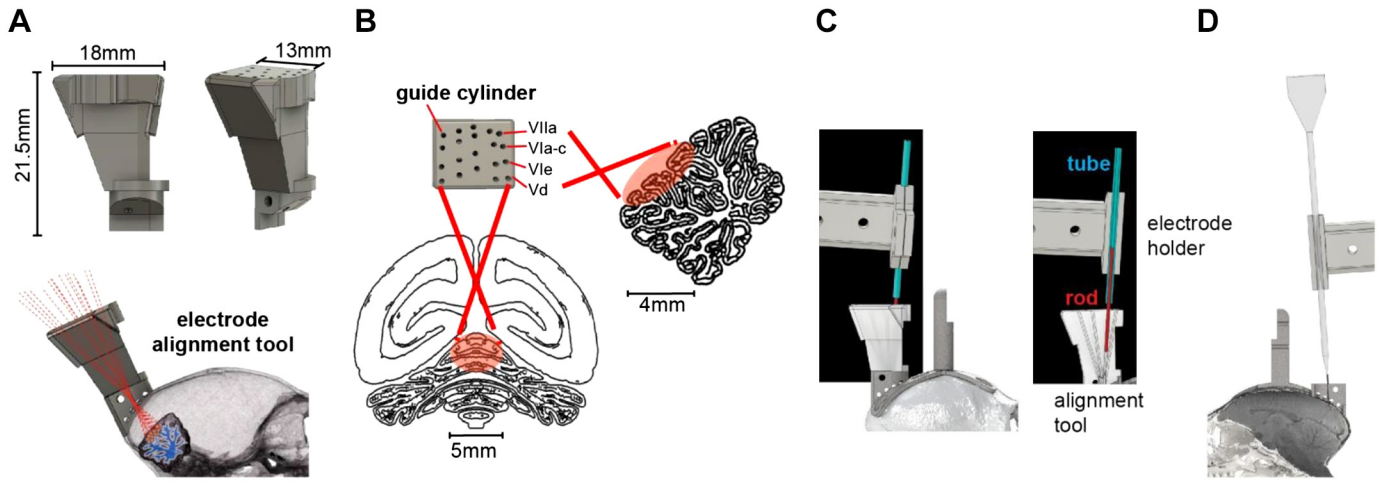

Fig. 3. Design of the electrode trajectory guidance tool. *A*: the alignment tool was designed to allow precise placement of the electrode along each of the 20 desired trajectories that converged onto various cerebellar destinations. The tool consisted of a 3-dimensionally (3D) printed block (2.03 g) that had a single cylinder for each of the desired electrode trajectories. Shown is a model of the tool with 20 guide cylinders that align with the recording regions of interest and converge through the single craniotomy burr hole. *B*: guide cylinder trajectories with posterior and sagittal views of the recording range on the cerebellum. Labels identify the cerebellar lobule that the trajectory is aimed toward. *C*: alignment of the electrode with the desired trajectory. We installed the alignment tool in the base chamber and then placed a rod in the cylinder corresponding to the desired trajectory (image at *right* shows a section view of the alignment tool). We then placed a tube in the electrode holder (the same holder that would later hold the electrode) and attached the electrode holder to the microdrive. The microdrive was then maneuvered by a micromanipulator so that the axis of motion of the microdrive holding the tube was aligned with the rod. *D*: an image of the electrode and the electrode holder aligned to advance along the desired trajectory.

models, creating an accurate representation of the distances and geometry of the desired cerebellar points, the desired burr hole, and the base chamber.

Using the coordinates of the various points, we created a set of 20 trajectories that originated from the desired recording locations in the cerebellum, converged through the single burr hole, and traveled out past the base chamber (Fig. 2*F*). Each line in 3D space represented a trajectory that an electrode would travel to reach a given cerebellar destination.

Design of an electrode guidance tool. Based on the electrode trajectories that we had defined in the postoperative model (Fig. 2*F*), we designed a tool that would be attached to the base chamber and provide alignment of the electrode to the specific trajectory that traveled through the burr hole and arrived at the desired cerebellar point of interest (Fig. 3*A*). This alignment tool featured 20 cylindrical tracks, each a cylinder of 1/32 in. in diameter. All cylinders converged onto the single burr hole, from which point the trajectories diverged to arrive at the various cerebellar destinations. The 20 cylinders (Fig. 3*B*, "guide cylinders") were configured in a 4×5 grid that corresponded to the four targeted cerebellar lobules (VIIa, VIa–c, VIe, and Vd), spanning from 0 to 2.5 mm along the midline-lateral axis. The cylinders in the alignment tool provided a physical representation of the electrode trajectories above the burr hole. The tool was 3D printed using an Objet260 printer with VeroClear plastic filament.

Alignment of the electrode. To advance the electrode, we chose a piezoelectric, high-precision microdrive (0.5-μm resolution) with an integrated absolute encoder (M3-LA-3.4-15 Linear Smart Stage; New Scale Technologies). The microdrive held the electrode and advanced it along a single axis defined by the chosen cylinder of the electrode alignment tool. Thus the next problem was to position the microdrive in 3D space so that its single direction of motion was precisely aligned with the desired cylinder in the electrode alignment tool.

To align the axis of the microdrive with the desired cylinder, we began by attaching the microdrive to a mechanical stereotaxic micromanipulator (SM-11-HT; Narishige, Japan). With the alignment tool installed in the base chamber, we inserted a 1/32-in. rod (outer diameter) inside the desired cylinder of the alignment tool (Fig. 3*C*) and then attached a 16-gauge tube (0.033-in. inner diameter) to the microdrive using the same electrode holder that would also hold the electrode. The tube was fixed to the microdrive, serving as a model for the axis of travel of the electrode.

We then used the stereotaxic micromanipulator to maneuver the microdrive, thereby positioning the tube held by the electrode holder so that it precisely traveled along the axis defined by the rod. Alignment of the tube (representing the electrode) with the rod (representing the guide) was confirmed under a microscope by advancing the microdrive and demonstrating that this motion inserted the rod into the tube. Once this alignment was confirmed, the stereotactic manipulator that held the microdrive was locked into place. We then removed the tube from the microdrive and replaced it with the recording electrode (Fig. 3*D*). All further motion of the electrode was now under the control of the microdrive, limited to a single axis of travel that was along the desired trajectory.

Craniotomy. Our design required that the 20 trajectories specified by the alignment tool converge on a single point on the skull and then travel within the brain to reach the cerebellum. The next step was to localize this point on the skull and drill a 1.5-mm diameter burr hole. This was achieved by using the alignment tool to mark the skull and localize the craniotomy. During the procedure the subject remained awake, following a protocol described earlier (Lu et al. 2001a).

The subject was head-fixed while the general craniotomy area, the base chamber, and the alignment tool were sterilized using alcohol, rinsed with saline, and then suctioned dry. The alignment tool was installed on the base chamber, and a 22-gauge blunt needle tip was dipped into ink and then inserted into one of the cylinders (the choice was arbitrary because all cylinders converged to the same burr hole location). The ink-tipped needle was advanced until contact was made with the bone, and a mark was left on the surface.

Using the procedures for aligning an electrode, we aligned a sterilized drill bit so that its trajectory of travel precisely matched the trajectory specified by a cylinder on the alignment tool. We attached a direct current motor to the bit and then attached the motor to the stereotaxic micromanipulator. At this point the alignment tool was removed, exposing the marked skull. From our coregistered pre- and postoperative CT, we estimated that the total thickness of the skull and dental cement was between 900 and 1,100 μm. Under a microscope, a miniature electric drill mounted on the micromanipulator was advanced to a near touch of the dental cement. The skull and dental cement thickness estimate were used to guide the advancement of the drill bit through the thin layer of dental cement and ~80–90% of the thickness of the bone (before reaching the dura). Drilling concluded with observation of wet bone chips and/or liquid. The remaining bone covering the dura surface was then carefully removed using handheld fine instruments under a microscope. Over the past two decades the Wang Laboratory (Lu et al. 2001a) has safely used this approach, and we were able to confirm that the animals never exhibited signs of discomfort or distress during this procedure.

Sealing the burr hole with a transparent silicone gel. Our design included a single burr hole, thus requiring us to continue using a single entry for many weeks during daily electrode penetrations. To accomplish this, we experimented with a silicone gel to seal the exposed dura at the burr hole.

Silicone gels can help preserve the integrity of the intracranial space after a craniotomy and prolong the life and functionality of burr holes. We wanted to use a gel that was nontoxic, transparent, elastic, easy to apply, and had resealing capabilities, allowing multiple penetrations by electrodes over an extended period of time.

We experimented with a commercially available soft silicone gel (DOWSIL 3-4680, Dow Corning; DuraGel, Cambridge Neurotech). This gel is a polydimethylsiloxane (PDMS)-based silicone and is primarily used for hydrophobic encapsulation of electronic microchips. However, because of its biocompatible and antibacterial properties, it recently has been used as a dura substitute/cover for chronic recording in mice (Jackson and Muthuswamy 2008; Jiang et al. 2017). These previous studies had tested biocompatibility, cytotoxicity, and sealing capability of the gel in mice, suggesting that it is a safe product, effective in sealing the dura from air contact, thereby minimizing possibility of infection. The published reports suggested that the gel had a number of attractive features: it was biocompatible, reduced possibility of inflammation, reduced cerebrospinal fluid leakage, reduced humidity loss from the craniotomy, and remained soft for a period of days to weeks, thereby allowing microelectrode penetration with minimal force.

Immediately after drilling the burr hole and cleaning the remaining bone chips, we covered the burr hole with the silicone gel (DuraGel; Cambridge Neurotech). Once the gel was cured (~30 min), its mechanical properties allowed the electrodes to penetrate it for weeks. Moreover, the viscosity of the gel allowed us to place it inside of the burr hole, thereby covering the dura completely, sealing it from air. The gel is transparent, which allowed us to monitor the dura beneath the gel. We replaced the gel at 2-wk intervals.

Data acquisition. We recorded from the cerebellum using three types of electrodes: quartz-insulated four-fiber (tetrode) or seven-fiber (heptode) metal core (platinum/tungsten 95/05) electrodes (Thomas Recording) and 64-contact high-density silicon probes (Cambridge Neurotech). None of these electrodes could penetrate the marmoset dura. Therefore, we performed a micro-durotomy using a 30-gauge needle, which was installed on the stereotaxic micromanipulator frame and advanced to the surface of dura until a puncture was made. Once the puncture was made, the various electrodes could travel through the dura.

We connected each electrode to a 32- or 64-channel head-stage amplifier and digitizer (Intan Technologies) and then connected the

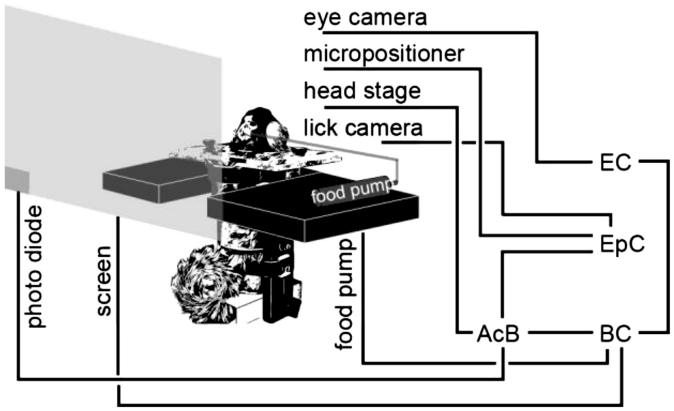

Fig. 4. Behavioral and electrophysiological recording system. AcB, acquisition board; BC, behavioral computer; EC, eye recording computer; EpC, electrophysiological computer.

head stage to a communication system (RHD2000; Intan Technologies), as shown in Fig. 4. In addition, we connected to the RHD2000 system digital outputs from our custom behavioral software and analog output from an optical sensor mounted on the monitor screen.

We used Open Ephys (Siegle et al. 2017), an open-source extracellular electrophysiology data acquisition software, for interfacing with the RHD2000 system and recording of signals. The signals were postprocessed and analyzed using MATLAB (The MathWorks, Natick, MA) and Python.

Behavioral training. In our earlier work in the macaque we had discovered that a key step in decoding activity of Purkinje cells in the oculomotor vermis was to organize them into groups in which all the cells within a group shared the same preference for visual error (Herzfeld et al. 2015, 2018). The preference for error was signaled via the cell's complex spike tuning, as measured when the animal made a saccade, but at saccade end the target was not on the fovea, resulting in a sensory prediction error that we represented as a vector. When the Purkinje cells were organized on the basis of their error-dependent complex spike tuning, each population predicted in real time the motion of the eyes during a saccade as a gain field. Thus we trained the marmosets in a task in which we could identify the complex spike tuning of each Purkinje cell with respect to visual error.

Immediately following surgical recovery, the animal was placed on a food-regulated diet. For 5 days/week, this diet consisted of 15 g of laboratory diet powder and 10 g of apple/mango sauce mixed in 30 g of water. This resulted in net 40 mL of deliverable food, which we administered via a syringe pump during the task. During the weekends, the food consisted of 30 g of a solid laboratory diet for the first day and 25 g for the second day.

Weight was monitored daily to ensure the health of the animals: weight was maintained within 85–100% of the average weight before the food regulation regime. If the weight fell below 85%, food regulation was stopped and the animal was fed in the colony until weight recovered to at least 90%. The animal was progressively acclimated to being held by a handler, entering its carrier independently, and sitting in its task chair. The experiment room was maintained at 74–84°F.

Saccade training proceeded at a frequency of 5 days/week. Visual targets were presented on a curved monitor (model AG32CQ, 32 in., 144 Hz; MSI) while binocular eye movements were tracked using an EyeLink 1000 eye tracking system (SR Research). We began with fixation training, followed by saccade training to a primary target. As the subject became accustomed to these paradigms, we introduced a secondary target, thus encouraging a corrective saccade (Fig. 5*A*).

Following fixation training, saccade training initiated with presentation of a primary target (0.5° × 0.5° square) at a random location and distance of 3°. Reward was provided if the primary saccade was within a 1.5° radius from the center of the primary target. In the fully trained subject, the trial began with fixation of a center target for 200 ms, after which a primary target (0.5° × 0.5° square) appeared at a random location at a distance of 5–6° (Fig. 5*A*). As the animal made a saccade to this primary target, that target was erased and a secondary

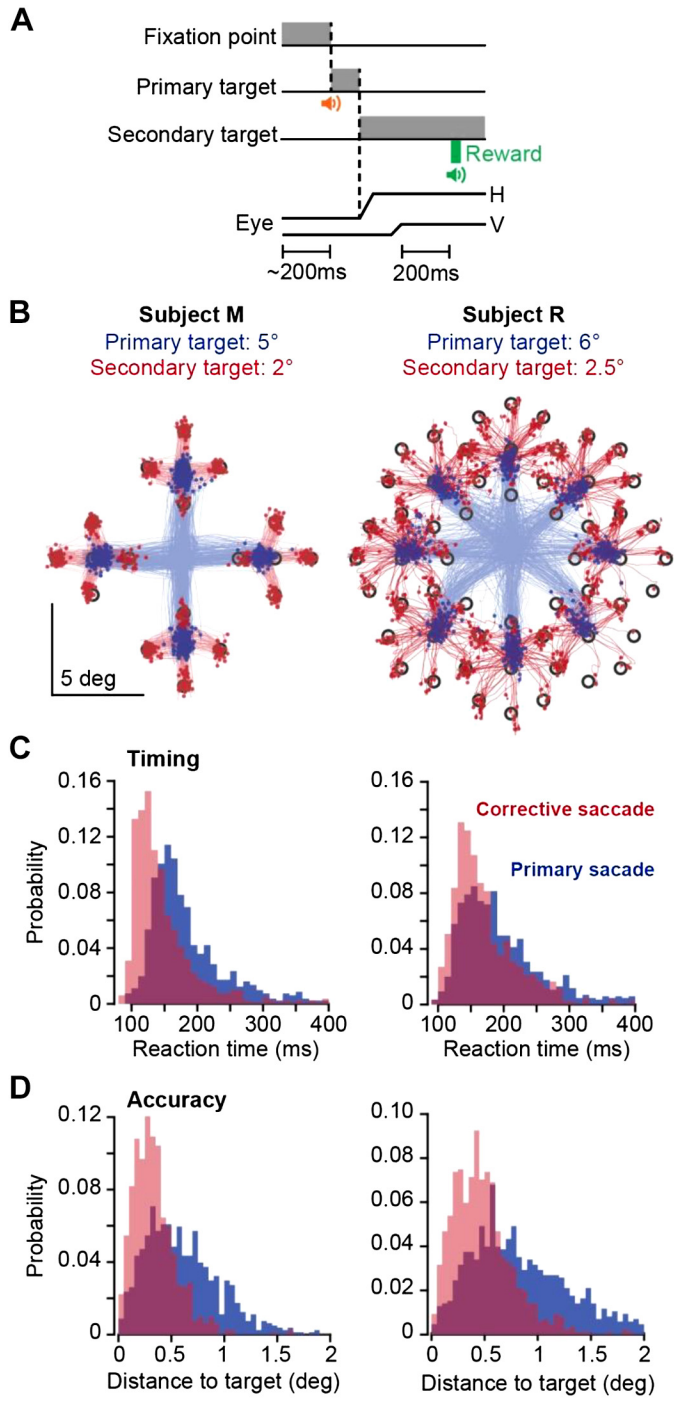

Fig. 5. Task design and behavioral results. *A*: a trial began with 200 ms of fixation, followed by presentation of a primary target at 5° or 6°. During the primary saccade, the target was erased and a secondary target was presented at 2° or 2.5° displacement with respect to the primary target. Reward was presented following 200-ms fixation of the secondary target. H, horizontal; V, vertical. *B*: saccade trajectories for *subjects M* and *R* during one session. Primary saccades are plotted in blue and corrective saccades in red. Targets were 0.5° × 0.5° square. *C*: reaction time distribution for primary and corrective saccades. *D*: distance to target at conclusion of primary and corrective saccades.

target was presented at a distance of 2–2.5°. The subject was rewarded if following the primary saccade it made a corrective saccade to the secondary target, landed within a 1.5° radius of the target center, and maintained fixation for 200 ms.

Correct trials produced a distinct auditory tone and engagement of the food pump at a rate of 0.020 mL/trial. We found that in the trained subjects, this low rate encouraged them to complete a few consecutive trials before stopping to lick the food tube, thus further increasing the number of correct trials per session.

Data analysis. To detect simple spikes, we began with a high-pass-filtered version of the signal (300 Hz) and then subtracted at each time point the mean of the signal across all contacts, a method known as common average referencing. We then used a threshold-based technique to hand sort the data. Here, we consider only the largest spike recorded by each contact. To detect complex spikes, we relied on frequency-domain analysis that tentatively identified these spikes via their power spectrum properties.

To confirm that the complex and simple spikes originated from the same cell, we compared the conditional probability Pr[$S(t)|C(0)$] with Pr[$S(t)|S(0)$]. These probabilities describe spike-triggered histograms. For example, Pr[$S(t)|C(0)$] is the probability that a simple spike occurred at time t, given that a complex spike was generated at *time 0*. Pr[$S(t)|S(0)$] is the probability that a simple spike occurred at time t, given that a simple spike was generated at *time 0*. Simple spikes that originate from a single cell produce a refractory period. Thus Pr[$S(t)|S(0)$] should exhibit a low-probability period of roughly 10 ms in duration centered at *time 0*. On the other hand, a complex spike suppresses production of future simple spikes, but not those that occurred before. As a result, Pr[$S(t)|C(0)$] should be asymmetric, with a long period of low simple spike probability following *time 0*.

Multicontact electrodes allow for analysis of simultaneously recorded neurons. However, spiking activity in one neuron can easily influence the data recorded by two nearby contacts, thus giving an illusion that the two contacts are picking up two distinct neurons. To guard against this, after we sorted the data in each contact, we waveform-triggered the data recorded by *contact A* by the spikes recorded on *contact B*. This identified the waveform of the neuron recorded by *contact B* on the spike recorded on *contact A*. We compared this cross-contact triggered waveform with the within-contact triggered waveform generated by the spikes recorded by *contact A*. The cross-contact triggered waveform should produce a different cluster of spikes in *A* than the main neuron isolated by *A*. If there were spikes that occurred within 1 ms of each other on *contacts A* and *B*, we used these coincident spike events to trigger the waveform in contact A. The spikes in *A* that were identified to be coincident with *B* should look approximately the same as the noncoincident spikes in *A*.

To quantify coordination between activities of two Purkinje cells, we computed conditional probabilities. For *contacts 1* and *2*, we computed Pr[$S(t)|C2(0)$], testing whether complex spikes on *contact 2* produced any changes in the simple spikes on *contact 1*. If the data were sorted properly, this conditional probability should be essentially flat. To visualize coordination between the neurons, we next plotted the spike-triggered waveform of voltages recorded by *contact 1*, triggered by the simple spikes on *contact 2*. Finally, we computed Pr[$S(t)|S2(0)$]. This measure quantified whether the occurrence of a simple spike on *contact 2* altered the probability of simple spikes on *contact 1*.

RESULTS

The methods that we described above allowed us to train subjects to produce ~1,000 trials per session during cerebellar recordings. However, we arrived at these methods following a learning process that involved a number of unsuccessful attempts. Below we describe our experience in terms of both types of results.

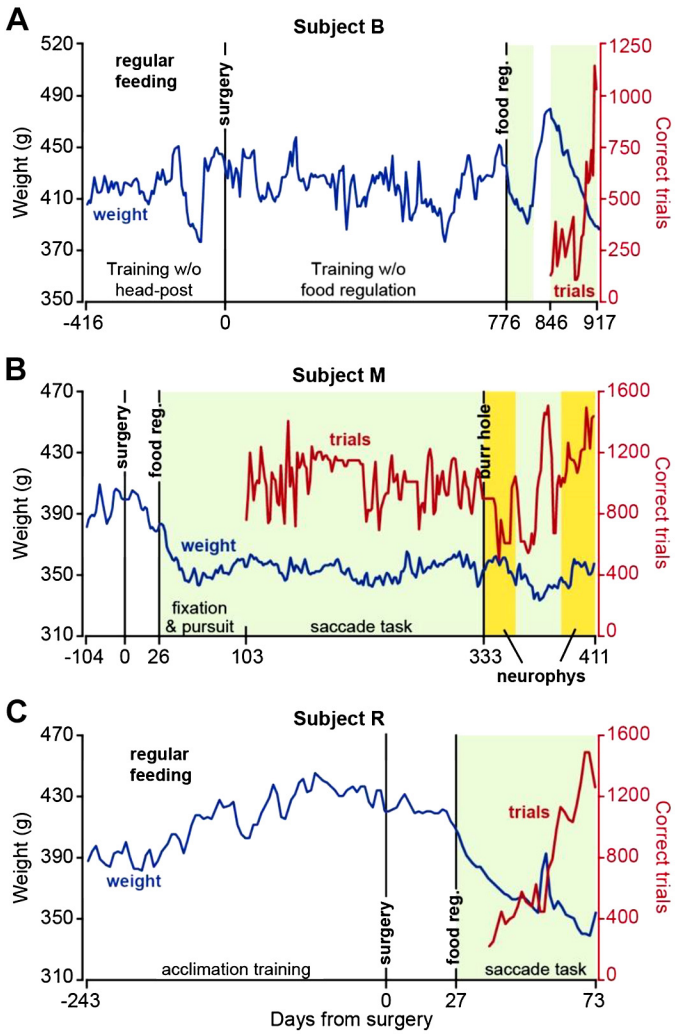

Fig. 6. Weight patterns and number of correct trials following food regulation. *A*: record of weight (blue) and correct trials (red) in *subject B*. Training began without a head post but was unsuccessful because of an inability to produce reliable calibration of eye measurements. Following surgery, a long period of training without food regulation ensued but was ultimately abandoned because of the unwillingness of the animal to work for more than a few hundred trials. Following food regulation, performance in the task dramatically improved. *B*: weight and correct trial data in *subject M*. *C*: weight and correct trial data in *subject R*. Data for correct trials represent a running average of bin size 2. Green shading indicates periods of food regulation. Yellow shading indicates periods of food regulation and neurophysiological recording.

Behavioral results. For *subject B*, we experimented with saccade training without the head post using a loose-fitting head-restraining system (Fig. 6*A*, *days −416* to *0*). Following a number of attempts, we abandoned this approach because we were unable to produce robust calibration.

We began behavioral training of *subject B* after head-post surgery, using the traditional method (Johnston et al. 2018; Mitchell et al. 2014) of feeding the animals in the colony and supplementing that food with reward during task performance in the head-fixed condition (Fig. 6*A*). We found that this was insufficient to motivate this subject.

We next eliminated home cage feeding on experiment days and instead provided task-based food rewards during the head-fixation period (Fig. 6). We ensured that regardless of performance, the subjects always received their required allotment of

food (at least 25 mL of food per day) and weight was maintained at around 90% of the pre-food regulation regime. However, food was delivered only while the animal was head-fixed. This produced improved performance in *subject B* (Fig. 6*A*, *days 846–917*). We then fully tested this approach in *subjects M* and *R* (Fig. 6, *B* and *C*, respectively).

Following recovery from surgery, *subject M* was food regulated and fed only in the head-fixed condition. After 30 sessions of fixation training, *subject M* was trained for 20 sessions on trials with primary saccades only (gradually increasing from 3° to 5°). Following this, *subject M* began training on the main task (Fig. 5*A*), which included both primary and corrective saccades. The number of correct trials shown in Fig. 6*B* begins with the first day of training on the primary saccade and continues as the subject transitioned to the main task. We found that within 3 mo after the start of fixation training, *subject M* was able to perform around 1,000 correct trials in the main task and then maintained this performance for over a year. During neurophysiological experiments, *subject M* produced 600–1,500 correct trials per session (neurophysiology trials, running average data presented in Fig. 6*B*).

We experimented with a different approach to saccade training in *subject R*. Instead of starting with fixation training, we began with pursuit training for 3 days. This subject's good performance allowed us to subsequently train on a saccade task for 15 sessions, during which only the primary target was presented and amplitude gradually increased from 3° to 5°. The subject was then trained on the main task (Fig. 5*A*), during which the primary target was placed at 6° and the secondary target at 2.5°. The number of correct trials in Fig. 6*C* begins with the first day of training on the primary saccade and continues as the subject graduated to the main task. This subject was able to produce 1,000–1,500 correct trials in the main task within 2 mo after food regulation (Fig. 6*C*).

Notably, during a year of food-regulated training in *subject M* and 2 mo of food-regulated training in *subject R*, both remained healthy, as suggested by their stable weight and lack of complications.

Our aim was to train the subjects in a task in which we could measure contributions of Purkinje cells to control of saccades. Each trial began with 200-ms fixation of a central location and was followed by a primary saccade to a peripheral target (y) at 5° or 6° displacement, corrective saccade to a secondary target at 2° or 2.5° displacement, and 200 ms of fixation at the secondary target (Fig. 5*A*). Saccades for a representative session are plotted in Fig. 5*B*, and the distribution of reaction times are plotted in Fig. 5*C*. Primary saccade reaction times for *subjects M* and *R* were 188 ± 65 and 197 ± 69 ms (means $\pm$ SD), respectively. Corrective saccade reaction times for *subjects M* and *R* were 146 ± 50 and 169 ± 50 ms, respectively. To quantify saccade accuracy, we measured the distance between saccade end point and target center and found that for the primary saccade, this distance was $0.59 \pm 0.35°$ for *subject M* and $0.85 \pm 0.50°$ for *subject R* (Fig. 5*D*). For the corrective saccade, distance to target was $0.34 \pm 0.22°$ for *subject M* and $0.49 \pm 0.32°$ for *subject R*. The reward region was a 1.5° radius around the target. As a result, across the two subjects, 81% (1,011 of 1,251) and 88% (1,464 of 1,672) of the trials that initiated with a primary saccade to the target concluded correctly and were rewarded.

An important component of our training was that the subjects received a small amount of food per correct trial: 0.02 mL per trial. At completion of a successful trial, the computer generated a beep and food delivery was signaled by the sound of the pump. However, the low reward rate encouraged the subjects to withhold licking until the food accumulated in the transparent tube that was placed in front of them. The effect was to teach the subjects to perform the task in blocks of three to four uninterrupted consecutive trials, thus increasing the total number of successful trials per session.

Simultaneous recordings from pairs of Purkinje cells. We explored lobules V, VI, and VII of the cerebellum using tetrodes, heptodes, and high-density silicon arrays. We thought that the cranial ground screw would be required to provide a reference for our electrophysiological recordings. However, with experience with *subject M*, we learned that the ground screw was unnecessary: the head post by itself acted as a reliable reference for the electrical signals during neurophysiological recordings. This is likely because the titanium screws established electrical continuity between the head post and the bone. Thus in *subject R* we eliminated the ground screw from the surgical procedures.

As the electrode approached the tentorium, there was a noticeable increase in background activity, indicative of proximity to Purkinje cells and their high baseline discharge rate. When the electrode passed through the tentorium, there was a distinct "pop," which was then followed by a gradual increase in spiking activity.

Identification of a Purkinje cell required the presence of both simple and complex spikes. Examples of putative complex and simple spikes, recorded by a silicon array, a tetrode, and a heptode, are presented in Fig. 7*A*. Complex spikes have a stereotypical positive wave that has slow dynamics, resulting in greater power in the lower frequencies (<300-Hz range) than the waveform of simple spikes (Warnaar et al. 2015). Furthermore, complex spikes are relatively rare events, presenting an interspike interval that is roughly two orders of magnitude greater than that of simple spikes.

A useful real-time tool for identification of complex spikes is a low-pass filter (300 Hz), which under good recording conditions can provide a tentative label for the complex spikes. Figure 7*B* shows an example of recording data from a heptode that simultaneously isolated three neurons: two putative Purkinje cells and a third unidentified neuron. The voltages for each of the three simultaneously recorded neurons are represented, as well as the low-pass-filtered version of the same signal. The complex spikes are tentatively identified by the sharp increase in the low-frequency power of the signal.

An important feature of a Purkinje cell is that production of a complex spike suppresses the generation of simple spikes for a period of 10 ms or longer. Thus the shared cellular origin of complex and simple spikes can be verified by using the complex spikes to trigger the voltage waveform. The *top* trace of Fig. 7*C* provides an example of this, demonstrating that the simple spikes occur with roughly equal probability before the complex spike, but then cease entirely after the complex spike.

We quantified this pattern via the condition probability $\Pr[S(t)|C(0)]$, which measured the probability of a simple spike at time t, given that a complex spike occurred at *time 0*. This measure illustrated that the simple spikes occurred with equal

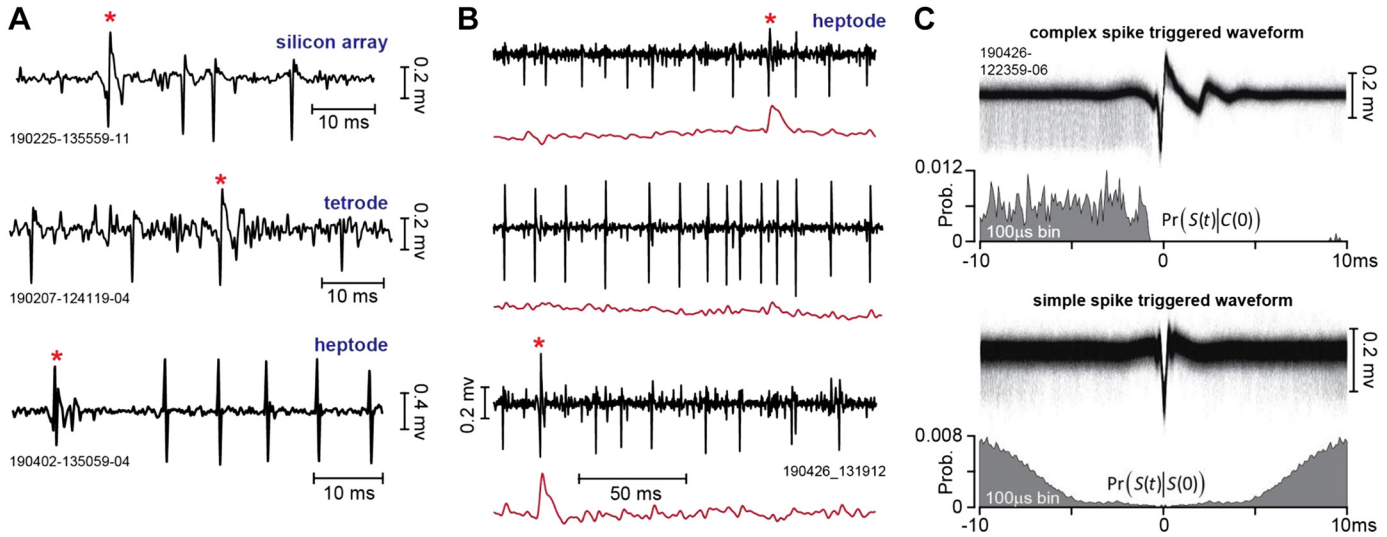

Fig. 7. Recordings from the marmoset cerebellum. *A*: complex and simple spikes recorded by a silicon array, a tetrode, and a heptode. The complex spike is noted by a red asterisk. *B*: example of multiple neurons simultaneously recorded by a heptode. Black traces are the high-pass-filtered voltages, and red traces are the low-pass-filtered versions of the same signal (300-Hz cutoff). *Top* and *bottom* traces are putative Purkinje cells; *middle* trace is an unidentified third neuron. *C*: spike-triggered waveforms and histograms. In the *top* trace, the voltages recorded by a single contact on a heptode were triggered by the complex spikes on the same contact. The resulting complex spike-triggered waveform exhibits a uniform pattern of simple spikes before the complex spike, and then simple spike suppression. This pattern is quantified as Pr[$S(t)|C(0)$], which is the probability of a simple spike at time t, given that a complex spike occurred at *time 0*. In the *bottom* trace, the voltages were triggered by the simple spikes. The resulting simple spike-triggered waveform exhibits a symmetric period of spike suppression, reflecting the Purkinje cell's refractory period. This pattern is quantified as Pr[$S(t)|S(0)$]. Prob., probability.

frequency before the complex spike but were then completely suppressed for ~10 ms following the complex spike.

A second feature of a Purkinje cell is that the simple spikes have a short refractory period. This feature can be verified by using the simple spikes to trigger the voltage waveform. The *bottom* trace of Fig. 7*C* provides an example of this. We quantified this pattern via the conditional probability Pr[$S(t)|S(0)$], which measured the probability of a simple spike at time t, given that a simple spike occurred at *time 0*. This measure illustrated that the simple spikes exhibited a 5-ms refractory period.

Two examples of simultaneously recorded neurons from lobule VII during the saccade task are shown in Fig. 8. In Fig. 8*A*, the heptode isolated three neurons, two of which were Purkinje cells. In this trial, the animal was presented with a target at 5° on the horizontal axis and made a saccade at 220-ms latency (Fig. 8*A*, *bottom*). At saccade onset the target was erased and redrawn at a displacement of 2° along the vertical axis. Thus, at the conclusion of the vertical saccade the target was not on the fovea, generating a visual error and encouraging the animal to make a corrective vertical saccade. This is an example of cross-axis adaptation (Deubel 1987; Xu-Wilson et al. 2009). The saccade landed ~0.5° short of the target and was followed by a corrective saccade. The Purkinje cell on *contact 6* (Fig. 8*A*) produced a complex spike before the primary saccade. A second Purkinje cell, recorded on *contact 5* (Fig. 8*A*), did not produce a complex spike before the onset of the primary saccade, but rather produced a complex spike following experience of a visual error (before onset of the corrective saccade). A third neuron was isolated by *contact 7*, but this neuron was not a Purkinje cell because it lacked complex spikes.

The waveforms for the complex and simple spikes in this recording session for each contact are shown in Fig. 8*B*, *left*. The waveforms illustrate the slower dynamics of the complex spikes, thus providing the basis for why a low-pass filter is generally useful in their identification.

Figure 8*B*, *middle*, displays the probability densities of the interspike intervals for each type of spike (note that the x-axis for the complex spikes is 5 s, whereas that for the simple spikes is 50 ms). The number of simple spikes in a given period of time was roughly two orders of magnitude larger than the number of complex spikes.

Figure 8*B*, *right*, illustrates the within-cell timing properties of the spikes via conditional probabilities. Pr[$S(t)|C(0)$] demonstrates that following a complex spike at *time 0*, there was a silent period of ~10 ms during which simple spikes were absent. Thus production of a complex spike briefly suppressed production of simple spikes, demonstrating that the complex and simple spikes on this contact originated from the same Purkinje cell. Pr[$S(t)|S(0)$] demonstrates a 5-ms refractory period, which is critical for demonstrating that the simple spikes were correctly attributed to a single Purkinje cell, and not misattributed because of cross-contaminated spikes from a neighboring contact. Finally, a comparison of Pr[$S(t)|C(0)$] with Pr[$S(t)|S(0)$] demonstrates that the complex-spike induced suppression of simple spikes was longer than the typical simple spike refractory period, another indication that the source of complex and simple spikes was a single Purkinje cell.

Another example of a recording session is shown in Fig. 8*C*. In this trial, the target was presented at 5° along the vertical axis and the animal made a saccade at a latency of 220 ms. At saccade onset, the primary target was erased and a new target at 2° to the right of the primary target was displayed. A Purkinje cell was isolated on *contact 1* while a second Purkinje cell was isolated on *contact 7*. *Contact 4* isolated a third neuron, but this was not a Purkinje cell.

Figure 8*D* illustrates the within-contact timing properties of the complex and simple spikes. Similarly to data in Fig. 8*B*, the conditional probabilities demonstrate that simple spikes exhib-

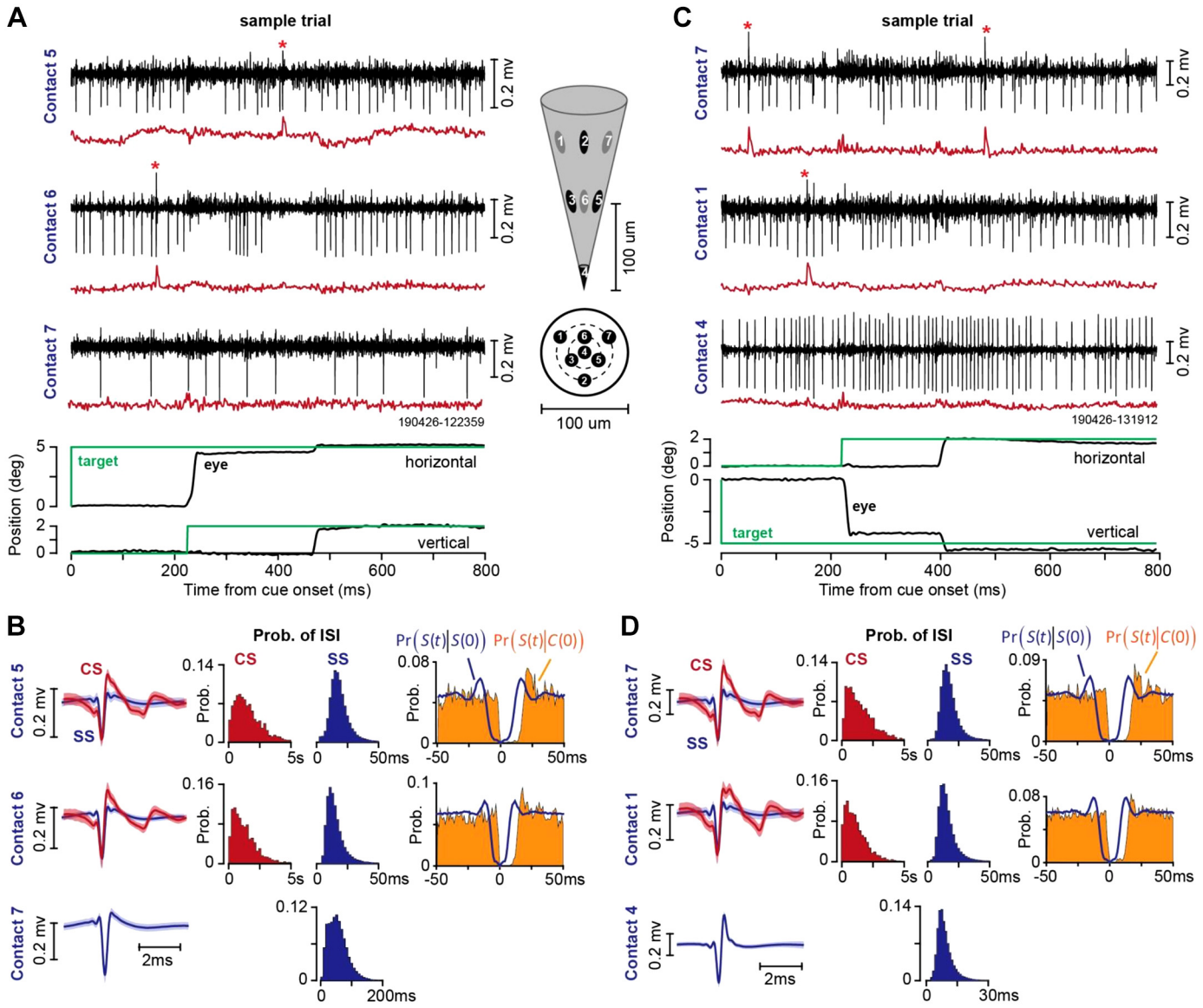

Fig. 8. Example of heptode recordings during two sessions in the saccade task. *A*: sample trial, illustrating activity of a Purkinje cell on *contact 5*, another Purkinje cell on *contact 6*, and an unidentified neuron on *contact 7*. Black traces are high-pass-filtered voltages, and red traces are low-passed-filtered signal (300-Hz cutoff). *Inset* shows the geometry of the heptode and the location of each contact. *B*: spike waveforms and patterns of spike timing recorded from the session in *A*. CS is complex spike, SS is simple spike, and ISI is interspike interval. Pr[$S(t)|S(0)$] is the probability of a simple spike at time t, given that a simple spike occurred at *time 0*. Pr[$S(t)|C(0)$] is the probability of a simple spike at time t, given that a complex spike occurred at *time 0*. *C*: sample trial recorded in a different session, illustrating activity of a Purkinje cell on *contact 7*, another Purkinje cell on *contact 1*, and an unidentified neuron on *contact 4*. *D*: spike waveforms and patterns of spike timing recorded from the session in *C*. Bin size is 1 ms for conditional probabilities, 200 ms for probability of complex spike ISI, and 2 ms for probability of simple spike ISI. Error bars on spike waveforms are SD. Prob., probability.

ited a 5-ms refractory period, and following a complex spike, there was suppression of simple spikes for a period of 10 ms.

In our experience, the head post and the electrode holder provided good recording stability. Over the course of 22 sessions in which single or pairs of Purkinje cells were isolated, we were able to maintain single-unit isolation during an average of 39.1 ± 3.8 min (mean ± SE), producing 516 ± 62 correct trials.

Activity of a Purkinje cell over the course of a representative session (700 trials, 40 min) is illustrated in Fig. 9. In this session, *subject M* performed the task shown in Fig. 5*B*. The trial began with a primary target at 5° displacement. On saccade initiation, the primary target was erased and replaced with a secondary target at 2° displacement (Fig. 9*A*). A corrective saccade followed termination of the primary saccade at a latency of 120–150 ms. The rasters in Fig. 9*A* present the timing of simple and complex spikes during each trial. This cell produced a burst of spikes around primary saccade onset, exhibiting elevated activity that continued long after the saccade had ended (Fig. 9*B*, *left*). There was a second burst of simple spikes around the time of the corrective saccade (Fig. 9*B*, *right*), which also exhibited a duration that was much longer than the saccade. This disparity between burst duration of simple spikes and duration of saccade is a common feature of saccade-related Purkinje cells (Herzfeld et al. 2015; Thier et al. 2000).

On termination of the primary saccade the target was not on the fovea, resulting in a sensory prediction error. This visual

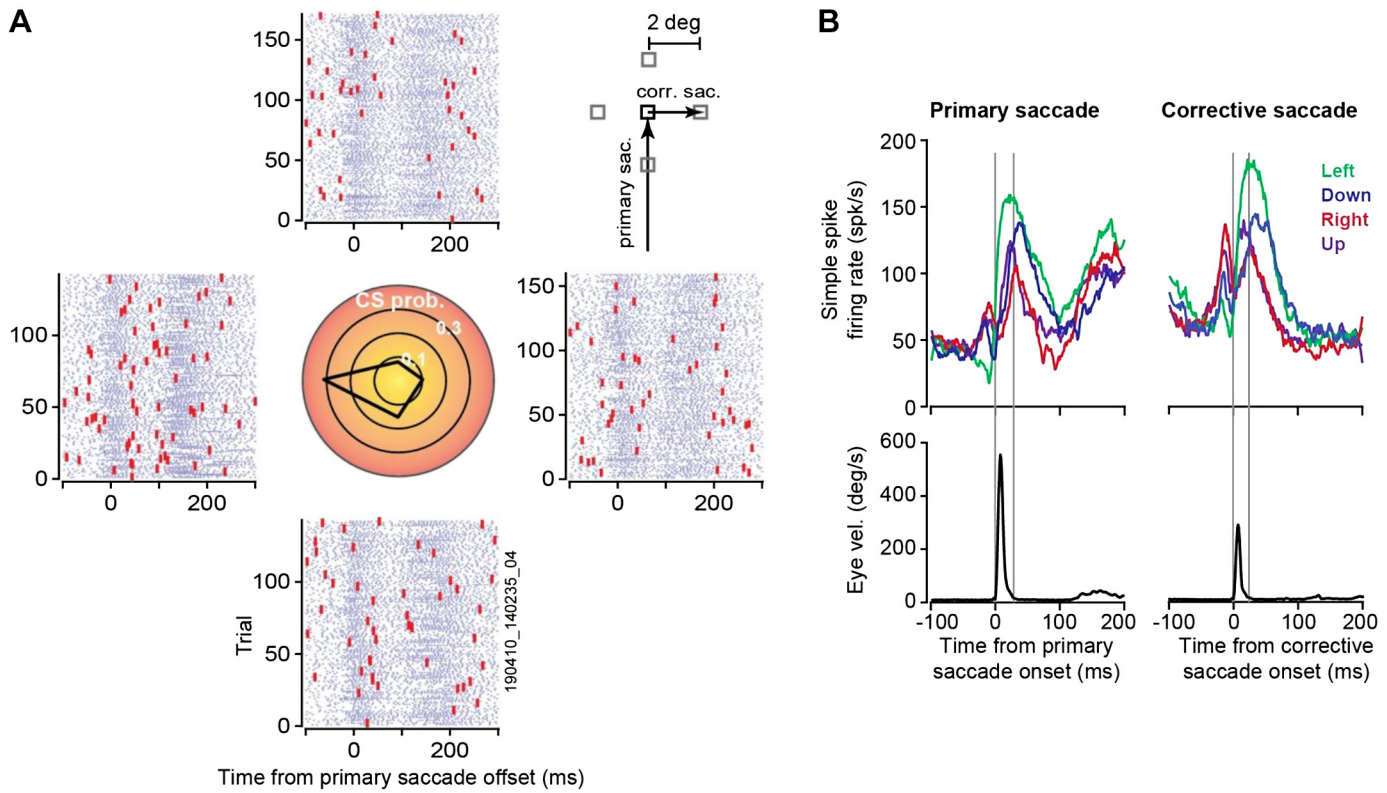

Fig. 9. Example of data recorded from a Purkinje cell (*subject M*) during the task shown in Fig. 5*B*. *A*: the primary target (black square, *inset*) was presented at 5° displacement. On initiation of saccade, the target was replaced with a secondary target (gray square, *inset*) at 2° displacement in 1 of 4 directions, inducing a visual error and encouraging a corrective saccade. Rasters are aligned to primary saccade offset and grouped on the basis of the direction of the visual error vector. For example, the rasters at *right* refer to trials in which the corrective saccade was to the right. The central plot shows probability of complex spikes during the 200-ms period following offset of the primary saccade. This cell had a preference for visual errors toward −180°. *B*: simple spike activity (*top*) and eye velocity (*bottom*) aligned to onset of primary saccade and corrective saccade. The simple spikes are grouped on the basis of direction of the primary saccade (left) or organized on the basis of direction of the corrective saccade (*right*). Gray vertical lines denote onset and offset of the saccade. The cell exhibited a burst of activity around saccade onset, but burst duration was much longer than saccade duration. corr. sac., Corrective saccade; primary sac., primary saccade; vel., velocity. CS prob., complex spike probability.

event likely engaged neurons in the superior colliculus (Kojima and Soetedjo 2017) and the inferior olive, leading to occasional complex spikes. We measured probability of complex spikes during the 200-ms period following completion of the primary saccade (Fig. 9*A*, *center*). This Purkinje cell was tuned to visual errors along −180°, suggesting that it received visual error information from the right superior colliculus via the left inferior olive.

Our earlier work (Herzfeld et al. 2015, 2018) found that when Purkinje cells are organized into populations that share a common preference for error (i.e., complex spike tuning is similar), their combined simple spike activity produces a pattern of spikes that no longer has a duration disparity with respect to the saccade. That is, whereas the simple spike activity of individual Purkinje cells does not have an obvious relationship to eye motion during a saccade, as a population the Purkinje cells can precisely predict motion of the eye in real time.

Spike-timing properties of simultaneously recorded Purkinje cells. The ability to record simultaneously from multiple Purkinje cells allows one to ask whether nearby cells coordinate their activity, a function that may be fundamental in driving neurons in the cerebellar nucleus (Person and Raman 2011). However, with multiple contacts there is a danger that some of the spikes that are recorded on *contact A* and attributed to Purkinje *cell 1* are in fact generated by nearby Purkinje *cell 2*, which in turn is also being recorded by *contact B*. This cross-contact influence (*cell 2* affecting recordings in both *contacts A* and *B*) would result in spurious coordination. One way to guard against this misattribution is to compare the spike-triggered waveforms.

Figure 10*A*, *left*, illustrates the waveform of simple spikes recorded by *contact 6* during the same session as that shown in Fig. 8*A*. Figure 10*A*, *middle*, illustrates the waveform recorded by *contact 6* but triggered by the simple spikes on *contact 5*. The data suggest that, on average, the voltages recorded by *contact 6* reflect in only a minor way the spikes being recorded by *contact 5*. Occasionally, the two Purkinje cells produced a simple spike within 1 ms of each other. The waveform on *contact 6* as triggered by only these synchronous events (Fig. 10*A*, *right*) looks very similar to the waveform of the usual spikes (Fig. 10*A*, *left*). Thus these features suggest that any coordinated activity present in the data of these two contacts would be because two independent cells fired simple spikes at approximately the same time.

We visualized the coordination between two Purkinje cells by triggering the voltages recorded by one contact via the simple spikes generated by a different Purkinje cell on a separate contact (Han et al. 2018). The resulting spike-triggered histogram of waveforms recorded by *contact 6*, triggered

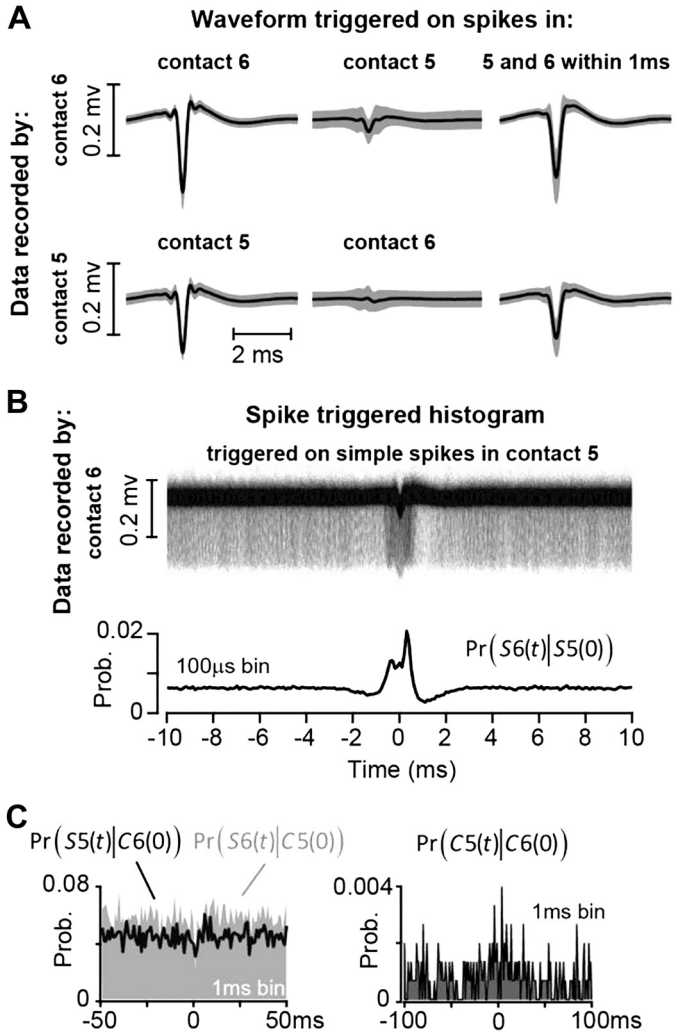

Fig. 10. Spike-timing property of a pair of simultaneously recorded Purkinje cells during the saccade task. *A*: a Purkinje cell was isolated by *contact 5* and another one by *contact 6*. Data recorded by *contact 6* (*top*) were triggered by simple spike events on *contact 6* (*left*) and by simple spike events on *contact 5* (*middle*); data on *right* were recorded by *contact 6* and triggered if there was a simple spike event in both *contacts 6* and *5* within 1 ms of each other. *Bottom* shows waveform for *contact 5*. On average, spikes in one contact did not produce a significant voltage change in another contact, and the shapes of synchronous (within 1 ms) and nonsynchronous spikes were nearly identical. *B*: to measure coordination among the Purkinje cells, we triggered the waveform on *contact 6* by the spikes on *contact 5*. The pattern of coordination is quantified via the conditional probability Pr[*S6*(*t*)|*S5*(0)]. *C*, *left*: the probability of simple spikes at time *t*, given that a complex spike occurred at *time 0* in another channel, quantified by Pr[*S5*(*t*)|*C6*(0)] and Pr[*S6*(*t*)|*C5*(0)]. There is no suppression of simple spikes following a complex spike. *Right*: the probability of co-occurrence of the complex spikes, Pr[*C5*(*t*)|*C6*(0)]. The 2 cells did not produce complex spikes that were strongly coordinated. Prob., probability.

by spikes on *contact 5*, is shown in Fig. 10*B*. The term Pr[*S6*(*t*)|*S5*(0)] measures the probability of simple spikes on *contact 6* at time *t*, given that a simple spike occurred on *contact 5* at *time 0*. The conditional probability exhibits a peak at around 0 ms, suggesting a measure of coordination. This coordination could have arisen because both Purkinje cells were saccade related, or driven by presentation of a visual stimulus. It is also possible that these two cells received similar inputs (Heck et al. 2007) or that activity in one affected activity in the other (Han et al. 2018).

Figure 10*C*, *left*, illustrates the spike-timing properties of these pairs of Purkinje cells. The conditional probability Pr[*S5*(*t*)|*C6*(0)] quantifies the effect of complex spikes on *contact 6* at *time 0* on the simple spikes on *contact 5* at *time t*. It demonstrates that the complex spike on *contact 6* did not suppress the simple spikes on *contact 5*. Similarly, the conditional probability Pr[*S6*(*t*)|*C5*(0)] demonstrates that the complex spike on *contact 5* did not suppress the simple spikes on *contact 6*. This provides further evidence that the two nearby contacts picked up two distinct Purkinje cells.

The conditional probability Pr[*C5*(*t*)|*C6*(0)], displayed in Fig. 10*C*, *right*, quantifies the relationship between complex spikes on *contacts 5* and *6*. This plot illustrates that the complex spikes in these two Purkinje cells were not well coordinated (little or no co-occurrence at 0-ms latency).

In summary, these data from a pair of simultaneously recorded Purkinje cells, cells that were likely less than 50 μm apart, suggest that the cells were not served by the same inferior olive neuron. However, the simple spikes exhibited a measure of coordination, suggesting that they may share common inputs or that the electrical activity in one cell influenced the activity in the other (Han et al. 2018).

Silicone gel coating of the burr hole. We sealed the burr hole with a silicone-based polymer (DuraGel) that we hoped would provide long-term protection to the dura while allowing for daily penetrations. Our experience with this product has been positive. Figure 11 provides images of the burr hole after drilling and following application of the gel. The gel remained in place for 2 wk as we performed daily recordings. At 2-wk intervals we removed the gel, examined the dura under a

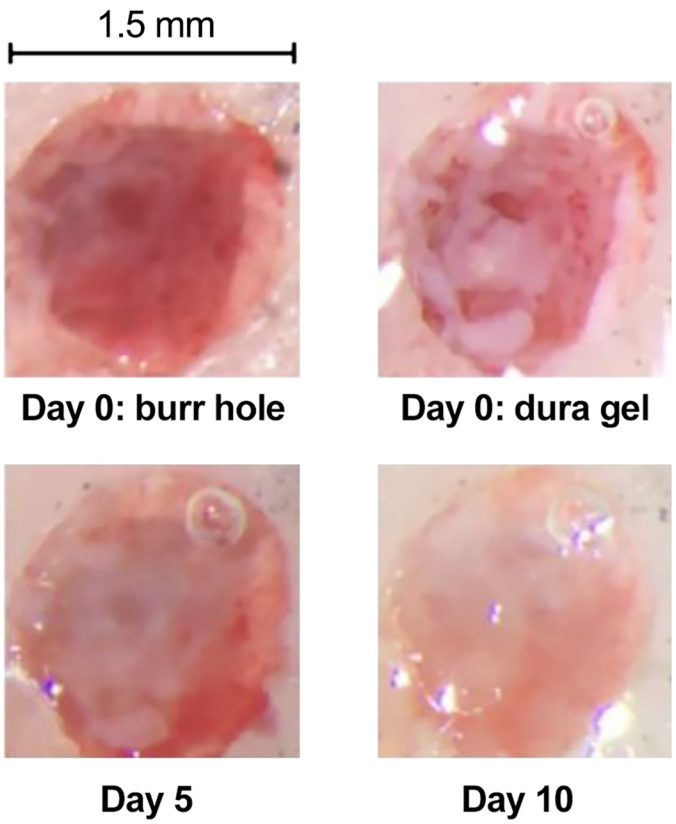

Fig. 11. Images from the burr hole before (*day 0*) and after application of the silicone gel.

microscope, and took samples and performed tissue culture. In every case the results suggested a healthy dura without any evidence of infection. Thus DuraGel appears compatible with the marmoset dura, providing long-term protection while allowing for daily electrode penetration.

DISCUSSION

Though the marmoset presents a number of attractive features as a primate model for the study of neural control of social behaviors, verbal communication, and saccadic eye movements, there is concern regarding whether the animals can be motivated to produce a sufficient number of trials. Previous reports on head-restrained marmosets have demonstrated operant conditioned behaviors in auditory tasks (Osmanski and Wang 2011; Osmanski et al. 2013; Remington et al. 2012) as well as eye movement tasks (Johnston et al. 2018; Mitchell et al. 2014). However, performance has been a concern: ~100 trials per session in the auditory task (Osmanski and Wang 2011; Osmanski et al. 2013; Remington et al. 2012), 80–100 trials per session in the saccade task (Johnston et al. 2018), and 300–800 trials per session in the eye movement task (Mitchell et al. 2014). In this study, we aimed to improve on these results and found that through a behavioral training protocol, it was possible to motivate the animals to consistently perform ~1,000 trials per session.

In addition, to investigate the neural basis of motor learning, we aimed to build tools that allowed for neurophysiological investigation of the cerebellum. We began with a CT- and MRI-based geometric model of the subject's skull and used that data to compute the curvature of the base of a 3D-printed titanium head post and chamber. Using the imaging data, we designed an alignment tool that had cylinders that guided an electrode through the burr hole via an absolute encoder microdrive. This resulted in stable recordings from multiple Purkinje cells during the saccade task.

Behavioral training. In previous reports, marmosets typically underwent a moderate food regulation regime and then were presented with the opportunity to acquire a form of liquid reward such as diluted apple sauce. In our approach, the subjects were gradually trained to receive their main source of nutrition as a consequence of rewarded behavior. Although our experience is limited to only three subjects, the results are encouraging: we were able to maintain the subjects in excellent health while motivating them to perform the task.

In previous reports, the amount of reward delivered per trial was relatively large: 0.1–0.2 mL per trial (Osmanski and Wang 2011; Osmanski et al. 2013; Remington et al. 2012), 0.07 mL per trial (Johnston et al. 2018), or 0.05–0.06 mL per trial (Mitchell et al. 2014). In the present study, we trained the subjects to expect a lower reward rate, 0.02 mL per trial. The sound of the successful trial and the engagement of the food pump indicated food delivery, but the low reward rate encouraged the subjects to wait three or more correct trials before harvesting the accumulated food. This low reward rate may have been an important factor in motivating the subjects to consistently produce a relatively large number of trials per session.

We were able to substantially reduce the training period in *subject R* by eliminating fixation training and instead starting with pursuit, finding that after only a few days it was possible to begin training on the saccade task and to arrive at ~1,000 correct trials within 1.5 mo after the start of food regulation.

Head post design. Our head post design departed significantly from the epoxy-based helmet design that has been employed in the past two decades in the study of the marmoset auditory cortex (Eliades and Wang 2008; Lu et al. 2001b; Roy and Wang 2012; Wang et al. 2005). Our design was made possible because of recent advances in 3D printing of titanium, allowing the use of imaging to build a subject-specific head post.

The X-shaped design of our head post was in contrast to the halo design recently demonstrated by the Everling group (Johnston et al. 2018) in the marmoset. Each design has its own advantages. The halo design maximizes the open surface of the skull, thus allowing for access to many regions of the brain, which is ideal for simultaneous recording from multiple cortical areas. In contrast, our X-shaped design limits the access to only the posterior regions but has the advantage that the animal's skin can cover the entire head post base, leaving only the chamber and the head post pole exposed. Thus our design allowed the skull to remain largely covered by skin.

Simultaneous recording from multiple Purkinje cells in the marmoset cerebellum. Although the marmoset is roughly the same weight as a rat, its cerebellum is about twice the size (Fujita et al. 2010). Similar to the rat, stripes of different aldolase C expression intensities separate the marmoset cerebellum into longitudinal compartments. However, olivo-cortical and cortico-nuclear projections indicate that the marmoset cerebellum has several compartments that are not present in rodents (compartments in the flocculus, nodulus, and the most lateral hemispheres; Fujita et al. 2010). Compared with the macaque, marmoset cerebellum has fewer folia but a relatively larger vermis. Because the vermis is likely the region critical for saccadic eye movements, as well as control of the tongue during vocalization, the marmoset vermis may be particularly well suited for study of internal models in motor control.

We found that with modern electrodes it was possible to isolate multiple Purkinje cells from the vermis during goal-directed saccades, something that to our knowledge has only once before been reported in the primate (Medina and Lisberger 2007). We have experimented with tetrodes, heptodes, and high-density silicon arrays, finding that each has its own advantages. Tetrodes and heptodes have a 3D geometry that gives them the potential to record from multiple Purkinje cells within the same folium, whereas silicon arrays provide the possibility to record from Purkinje cells across folia. In our hands, the 3D geometry of the heptode has provided a robust ability to routinely isolate and stably maintain recording from pairs of Purkinje cells. These cells often share important functional properties such as complex spike tuning and simple spike coordination (Fig. 10).

We also found that the computational tools used for identifying Purkinje cells in other animals worked well in the marmoset. As in other animals, the complex spikes in the marmoset Purkinje cells had a waveform that exhibited slow dynamics, making it possible to use frequency-based filtering techniques to tentatively distinguish complex spikes from simple spikes. Furthermore, following a complex spike, there was a 10- to 15-ms period of simple spike suppression, helping to confirm that a single Purkinje cell produced both spikes.

Finally, we were able to simultaneously record from pairs of Purkinje cells and observe submillisecond coordination in their timing. Populations of Purkinje cells can coordinate their spiking, and this coordination may play a critical role in regulating activity of neurons in the deep cerebellar nucleus (Person and Raman 2011). Perhaps the earliest demonstration of simple spike coordination was by Bell and Grimm (1969), who made microelectrode recordings in anesthetized cats, finding that Purkinje cells that were located <70 μm apart often fired nearly simultaneously. Later work found further evidence in support of this idea (De Zeeuw et al. 1997; Ebner and Bloedel 1981; Heck et al. 2007; Shin and De Schutter 2006; Wise et al. 2010). For example, Heck et al. (2007) demonstrated that in rats, Purkinje cells within a few hundred micrometers fired synchronously during the period of reach to grasp of a food pellet, but not during the period after grasp completion.

In the present study we observed some evidence for submillisecond coordination in simple spikes of nearby Purkinje cells during performance of a saccade task. A recent study in mice (Han et al. 2018) also found that firing of many neighboring Purkinje cells exhibited submillisecond coordination. That study noted that when chemical synapses were blocked in brain slices, some synchrony persisted. They suggested that submillisecond coordination of neighboring Purkinje cells was not via shared synaptic inputs, but via electrical activity that in one Purkinje cell resulted in opening of sodium channels in the neighboring Purkinje cell. The question of whether Purkinje cells in the primate produce coordinated activity during goal-directed movements remains to be explored.

The need to record from Purkinje cells during sensorimotor learning. For accurate movements, the brain relies on the cerebellum to build internal models and predict sensory consequences of motor commands (Donchin et al. 2012; Golla et al. 2008; Izawa et al. 2012; Maschke et al. 2004; Rabe et al. 2009; Roth et al. 2013 Smith and Shadmehr 2005). However, it has been difficult to decipher how the cerebellum learns internal models because the neural encoding of movements has been difficult to decode in the simple spikes of Purkinje cells (Helmchen and Büttner 1995; Hewitt et al. 2011; Roitman et al. 2005, 2009; Thier et al. 2000). Because learning produces a change in the neural coding, this poor understanding has made it difficult to relate the rich behavioral changes that have been observed during motor learning, such as multiple timescales of memory (Kording et al. 2007; Smith et al. 2006), spontaneous recovery (Ethier et al. 2008), and savings (Pekny et al. 2011), with the neural mechanisms of learning in the cerebellum. Our long-term goal in building this marmoset laboratory is to search for the neural basis of learning internal models. However, the first step is to understand the neural code with which Purkinje cells make predictions.

Recently, using data in the macaque, we proposed that the Purkinje cells may be organized in micro-clusters (Herzfeld et al. 2015, 2018), wherein each micro-cluster is composed of Purkinje cells that share a common preference for error. The preference for error is expressed through the complex spike tuning of the Purkinje cell (Soetedjo and Fuchs 2006; Soetedjo et al. 2008). We found that if Purkinje cells were organized in this way, the language of internal models as expressed by Purkinje cells became decipherable: simple spikes as a population predicted the real-time motion of the eye during a saccade (Herzfeld et al. 2015). Thus this theory suggested a potential solution to the encoding problem: organize the simple spikes of a population of Purkinje cells on the basis of the functional properties of each cell's complex spikes.

If the neural representation of internal model relies on a population coding of Purkinje cells, the challenge is to simultaneously record simple and complex spikes from multiple Purkinje cells in the awake, behaving animals. However, this has proven to be difficult. Array electrodes have simultaneously isolated multiple Purkinje cells in rodents (Blenkinsop and Lang 2011; Sugihara et al. 2007; Tang et al. 2016, 2019; Welsh et al. 1995) and decerebrated cats (Ebner and Bloedel 1981), but this has often been in the anesthetized animal (however, see Han et al. 2018). In the awake, behaving subject, calcium imaging has been used to track complex spikes in multiple Purkinje cells (Kostadinov et al. 2019; Najafi et al. 2014), but this technique does not yet have the temporal resolution to track simple spikes. In primates, simultaneous recordings from Purkinje cells are quite rare. Until our work, the report by Medina and Lisberger (2007) is the only example we are aware of in which pairs of Purkinje cells were recorded in the primate during goal-directed behavior.

Limitations. Although the X-shaped head post design had the advantage that the skin would cover nearly the entire skull, we found that within about a year following surgery the skin in *subjects B* and *M* gradually receded to the boundary of the dental cement. One of our challenges is to find ways to slow and eventually prevent this process of skin contraction, which might include experimentation with different forms of cement or its elimination.

Our experience with array-type electrodes that have contacts along a single surface suggests that despite their high density, these electrodes can provide isolation of multiple Purkinje cells along neighboring folia, but rarely within a single folium. The goal of simultaneously recording from many Purkinje cells within a single folium will likely require employment of multiple electrodes.

Isolation of multiple Purkinje cells introduces the computational problem of spike attribution, given that one contact can record complex spikes whereas the other records only simple spikes. In this study, we showed that conditional probabilities that consider the effect of complex spikes on simple spikes can help with the attribution problem, but the task becomes much harder when many contacts are involved.

In summary, to better understand the neural basis of internal models, we have built a new laboratory that focuses on marmosets. We have reported our attempts to improve marmoset behavioral training and electrophysiological recording methods. We found that through behavioral shaping, it was possible to motivate the animals to perform ~1,000 trials in a head-fixed saccade task. We also found that with the aid of imaging, it was possible to build a system for simultaneous isolation of multiple Purkinje cells in the cerebellum.

ACKNOWLEDGMENTS

We are grateful to Tahl Holtzman from Cambridge Neurotech, who made important suggestions regarding choice of microdrive, electrodes, and silicone gel for protection of the dura. We are also grateful to Mehrdad Jazayeri and Mark Churchland, who gave invaluable advice on design of the laboratory. We are very grateful to Seth Koehler, Xiao-Ping Liu, and Wang Laboratory technicians for helping with surgeries and animal care.

Present address of D. J. Herzfeld: Dept. of Neurobiology, Duke University School of Medicine, Durham, NC 27710 (e-mail: herzfeldd@gmail.com).

GRANTS

The work was supported by National Institute of Neurological Disorders and Stroke Grant 5R01NS078311, Office of Naval Research Grant N00014-15-1-2312, and National Science Foundation Grant CNS-1714623.

DISCLOSURES

No conflicts of interest, financial or otherwise, are declared by the authors.

AUTHOR CONTRIBUTIONS

D.J.H., P.H., K.K., T.P., X.W., and R.S. conceived and designed research; E.S.-N., D.J.H., and P.H. performed experiments; E.S.-N. and K.K. analyzed data; E.S.-N., K.K., and R.S. interpreted results of experiments; E.S.-N., P.H., and T.P. prepared figures; P.H. and R.S. drafted manuscript; D.J.H. and R.S. edited and revised manuscript; R.S. approved final version of manuscript.

REFERENCES

Barash S, Melikyan A, Sivakov A, Zhang M, Glickstein M, Thier P. Saccadic dysmetria and adaptation after lesions of the cerebellar cortex. *J Neurosci* 19: 10931–10939, 1999. doi:10.1523/JNEUROSCI.19-24-10931.1999.

Bell CC, Grimm RJ. Discharge properties of Purkinje cells recorded on single and double microelectrodes. *J Neurophysiol* 32: 1044–1055, 1969. doi:10.1152/jn.1969.32.6.1044.

Blenkinsop TA, Lang EJ. Synaptic action of the olivocerebellar system on cerebellar nuclear spike activity. *J Neurosci* 31: 14708–14720, 2011. doi:10.1523/JNEUROSCI.3323-11.2011.

Cajal SR. *Recollections of My Life*. Cambridge, MA: MIT Press, 1989.

Courchesne E, Karns CM, Davis HR, Ziccardi R, Carper RA, Tigue ZD, Chisum HJ, Moses P, Pierce K, Lord C, Lincoln AJ, Pizzo S, Schreibman L, Haas RH, Akshoomoff NA, Courchesne RY. Unusual brain growth patterns in early life in patients with autistic disorder: an MRI study. *Neurology* 57: 245–254, 2001. doi:10.1212/WNL.57.2.245.

De Zeeuw CI, Koekkoek SK, Wylie DR, Simpson JI. Association between dendritic lamellar bodies and complex spike synchrony in the olivocerebellar system. *J Neurophysiol* 77: 1747–1758, 1997. doi:10.1152/jn.1997.77.4.1747.

Deubel H. Adaptivity of gain and direction in oblique saccades. In: *Eye Movements: From Physiology to Cognition*, edited by O'Regan JK, Levy-Schoen A. New York: Elsevier, 1987, p. 181–190.

Donchin O, Rabe K, Diedrichsen J, Lally N, Schoch B, Gizewski ER, Timmann D. Cerebellar regions involved in adaptation to force field and visuomotor perturbation. *J Neurophysiol* 107: 134–147, 2012. doi:10.1152/jn.00007.2011.

Ebner TJ, Bloedel JR. Correlation between activity of Purkinje cells and its modification by natural peripheral stimuli. *J Neurophysiol* 45: 948–961, 1981. doi:10.1152/jn.1981.45.5.948.

Eliades SJ, Miller CT. Marmoset vocal communication: behavior and neurobiology. *Dev Neurobiol* 77: 286–299, 2017. doi:10.1002/dneu.22464.

Eliades SJ, Wang X. Chronic multi-electrode neural recording in free-roaming monkeys. *J Neurosci Methods* 172: 201–214, 2008. doi:10.1016/j.jneumeth.2008.04.029.

Eliades SJ, Wang X. Comparison of auditory-vocal interactions across multiple types of vocalizations in marmoset auditory cortex. *J Neurophysiol* 109: 1638–1657, 2013. doi:10.1152/jn.00698.2012.

Ethier V, Zee DS, Shadmehr R. Spontaneous recovery of motor memory during saccade adaptation. *J Neurophysiol* 99: 2577–2583, 2008. doi:10.1152/jn.00015.2008.

Fedorov A, Beichel R, Kalpathy-Cramer J, Finet J, Fillion-Robin JC, Pujol S, Bauer C, Jennings D, Fennessy F, Sonka M, Buatti J, Aylward S, Miller JV, Pieper S, Kikinis R. 3D Slicer as an image computing platform for the Quantitative Imaging Network. *Magn Reson Imaging* 30: 1323–1341, 2012. doi:10.1016/j.mri.2012.05.001.

Fujita H, Oh-Nishi A, Obayashi S, Sugihara I. Organization of the marmoset cerebellum in three-dimensional space: lobulation, aldolase C compartmentalization and axonal projection. *J Comp Neurol* 518: 1764–1791, 2010. doi:10.1002/cne.22301.

Golla H, Tziridis K, Haarmeier T, Catz N, Barash S, Thier P. Reduced saccadic resilience and impaired saccadic adaptation due to cerebellar disease. *Eur J Neurosci* 27: 132–144, 2008. doi:10.1111/j.1460-9568.2007.05996.x.

Han KS, Guo C, Chen CH, Witter L, Osorno T, Regehr WG. Ephaptic coupling promotes synchronous firing of cerebellar Purkinje cells. *Neuron* 100: 564–578.e3, 2018. doi:10.1016/j.neuron.2018.09.018.

Hashimoto T, Tayama M, Murakawa K, Yoshimoto T, Miyazaki M, Harada M, Kuroda Y. Development of the brainstem and cerebellum in autistic patients. *J Autism Dev Disord* 25: 1–18, 1995. doi:10.1007/BF02178163.

Heck DH, Thach WT, Keating JG. On-beam synchrony in the cerebellum as the mechanism for the timing and coordination of movement. *Proc Natl Acad Sci USA* 104: 7658–7663, 2007. doi:10.1073/pnas.0609966104.

Helmchen C, Büttner U. Saccade-related Purkinje cell activity in the oculomotor vermis during spontaneous eye movements in light and darkness. *Exp Brain Res* 103: 198–208, 1995. doi:10.1007/BF00231706.

Herzfeld DJ, Kojima Y, Soetedjo R, Shadmehr R. Encoding of action by the Purkinje cells of the cerebellum. *Nature* 526: 439–442, 2015. doi:10.1038/nature15693.

Herzfeld DJ, Kojima Y, Soetedjo R, Shadmehr R. Encoding of error and learning to correct that error by the Purkinje cells of the cerebellum. *Nat Neurosci* 21: 736–743, 2018. doi:10.1038/s41593-018-0136-y.

Hewitt AL, Popa LS, Pasalar S, Hendrix CM, Ebner TJ. Representation of limb kinematics in Purkinje cell simple spike discharge is conserved across multiple tasks. *J Neurophysiol* 106: 2232–2247, 2011. doi:10.1152/jn.00886.2010.

Izawa J, Criscimagna-Hemminger SE, Shadmehr R. Cerebellar contributions to reach adaptation and learning sensory consequences of action. *J Neurosci* 32: 4230–4239, 2012. doi:10.1523/JNEUROSCI.6353-11.2012.

Jackson N, Muthuswamy J. Artificial dural sealant that allows multiple penetrations of implantable brain probes. *J Neurosci Methods* 171: 147–152, 2008. doi:10.1016/j.jneumeth.2008.02.018.

Jiang Z, Huxter JR, Bowyer SA, Blockeel AJ, Butler J, Imtiaz SA, Wafford KA, Phillips KG, Tricklebank MD, Marston HM, Rodriguez-Villegas E. TaiNi: maximizing research output whilst improving animals' welfare in neurophysiology experiments. *Sci Rep* 7: 8086, 2017. doi:10.1038/s41598-017-08078-8.

Johnston KD, Barker K, Schaeffer L, Schaeffer D, Everling S. Methods for chair restraint and training of the common marmoset on oculomotor tasks. *J Neurophysiol* 119: 1636–1646, 2018. doi:10.1152/jn.00866.2017.

Kishi N, Sato K, Sasaki E, Okano H. Common marmoset as a new model animal for neuroscience research and genome editing technology. *Dev Growth Differ* 56: 53–62, 2014. doi:10.1111/dgd.12109.

Kojima Y, Soetedjo R. Change in sensitivity to visual error in superior colliculus during saccade adaptation. *Sci Rep* 7: 9566, 2017. doi:10.1038/s41598-017-10242-z.

Kording KP, Tenenbaum JB, Shadmehr R. The dynamics of memory as a consequence of optimal adaptation to a changing body. *Nat Neurosci* 10: 779–786, 2007. doi:10.1038/nn1901.

Kostadinov D, Beau M, Pozo MB, Häusser M. Predictive and reactive reward signals conveyed by climbing fiber inputs to cerebellar Purkinje cells. *Nat Neurosci* 22: 950–962, 2019. doi:10.1038/s41593-019-0381-8.

Lu T, Liang L, Wang X. Neural representations of temporally asymmetric stimuli in the auditory cortex of awake primates. *J Neurophysiol* 85: 2364–2380, 2001a. doi:10.1152/jn.2001.85.6.2364.

Lu T, Liang L, Wang X. Temporal and rate representations of time-varying signals in the auditory cortex of awake primates. *Nat Neurosci* 4: 1131–1138, 2001b. doi:10.1038/nn737.

MacDougall M, Nummela SU, Coop S, Disney A, Mitchell JF, Miller CT. Optogenetic manipulation of neural circuits in awake marmosets. *J Neurophysiol* 116: 1286–1294, 2016. doi:10.1152/jn.00197.2016.

Marko MK, Crocetti D, Hulst T, Donchin O, Shadmehr R, Mostofsky SH. Behavioural and neural basis of anomalous motor learning in children with autism. *Brain* 138: 784–797, 2015. doi:10.1093/brain/awu394.

Maschke M, Gomez CM, Ebner TJ, Konczak J. Hereditary cerebellar ataxia progressively impairs force adaptation during goal-directed arm movements. *J Neurophysiol* 91: 230–238, 2004. doi:10.1152/jn.00557.2003.

Medina JF, Lisberger SG. Variation, signal, and noise in cerebellar sensory-motor processing for smooth-pursuit eye movements. *J Neurosci* 27: 6832–6842, 2007. doi:10.1523/JNEUROSCI.1323-07.2007.

Miller CT, Freiwald WA, Leopold DA, Mitchell JF, Silva AC, Wang X. Marmosets: a neuroscientific model of human social behavior. *Neuron* 90: 219–233, 2016. doi:10.1016/j.neuron.2016.03.018.

Mitchell JF, Reynolds JH, Miller CT. Active vision in marmosets: a model system for visual neuroscience. *J Neurosci* 34: 1183–1194, 2014. doi:10.1523/JNEUROSCI.3899-13.2014.

Murakami JW, Courchesne E, Press GA, Yeung-Courchesne R, Hesselink JR. Reduced cerebellar hemisphere size and its relationship to vermal hypoplasia in autism. *Arch Neurol* 46: 689–694, 1989. doi:10.1001/archneur.1989.00520420111032.

Mustoe AC, Cavanaugh J, Harnisch AM, Thompson BE, French JA. Do marmosets care to share? Oxytocin treatment reduces prosocial behavior toward strangers. *Horm Behav* 71: 83–90, 2015. doi:10.1016/j.yhbeh.2015.04.015.

Najafi F, Giovannucci A, Wang SS, Medina JF. Sensory-driven enhancement of calcium signals in individual Purkinje cell dendrites of awake mice. *Cell Reports* 6: 792–798, 2014. doi:10.1016/j.celrep.2014.02.001.

Osmanski MS, Song X, Wang X. The role of harmonic resolvability in pitch perception in a vocal nonhuman primate, the common marmoset (*Callithrix jacchus*). *J Neurosci* 33: 9161–9168, 2013. doi:10.1523/JNEUROSCI.0066-13.2013.

Osmanski MS, Wang X. Measurement of absolute auditory thresholds in the common marmoset (*Callithrix jacchus*). *Hear Res* 277: 127–133, 2011. doi:10.1016/j.heares.2011.02.001.

Pekny SE, Criscimagna-Hemminger SE, Shadmehr R. Protection and expression of human motor memories. *J Neurosci* 31: 13829–13839, 2011. doi:10.1523/JNEUROSCI.1704-11.2011.

Person AL, Raman IM. Purkinje neuron synchrony elicits time-locked spiking in the cerebellar nuclei. *Nature* 481: 502–505, 2011. doi:10.1038/nature10732.

Rabe K, Livne O, Gizewski ER, Aurich V, Beck A, Timmann D, Donchin O. Adaptation to visuomotor rotation and force field perturbation is correlated to different brain areas in patients with cerebellar degeneration. *J Neurophysiol* 101: 1961–1971, 2009. doi:10.1152/jn.91069.2008.

Remington ED, Osmanski MS, Wang X. An operant conditioning method for studying auditory behaviors in marmoset monkeys. *PLoS One* 7: e47895, 2012. doi:10.1371/journal.pone.0047895.

Roitman AV, Pasalar S, Ebner TJ. Single trial coupling of Purkinje cell activity to speed and error signals during circular manual tracking. *Exp Brain Res* 192: 241–251, 2009. doi:10.1007/s00221-008-1580-9.

Roitman AV, Pasalar S, Johnson MT, Ebner TJ. Position, direction of movement, and speed tuning of cerebellar Purkinje cells during circular manual tracking in monkey. *J Neurosci* 25: 9244–9257, 2005. doi:10.1523/JNEUROSCI.1886-05.2005.

Roth MJ, Synofzik M, Lindner A. The cerebellum optimizes perceptual predictions about external sensory events. *Curr Biol* 23: 930–935, 2013. doi:10.1016/j.cub.2013.04.027.

Roy S, Miller CT, Gottsch D, Wang X. Vocal control by the common marmoset in the presence of interfering noise. *J Exp Biol* 214: 3619–3629, 2011. doi:10.1242/jeb.056101.

Roy S, Wang X. Wireless multi-channel single unit recording in freely moving and vocalizing primates. *J Neurosci Methods* 203: 28–40, 2012. doi:10.1016/j.jneumeth.2011.09.004.

Sasaki E, Suemizu H, Shimada A, Hanazawa K, Oiwa R, Kamioka M, Tomioka I, Sotomaru Y, Hirakawa R, Eto T, Shiozawa S, Maeda T, Ito M, Ito R, Kito C, Yagihashi C, Kawai K, Miyoshi H, Tanioka Y, Tamaoki N, Habu S, Okano H, Nomura T. Generation of transgenic non-human primates with germline transmission. *Nature* 459: 523–527, 2009. doi:10.1038/nature08090.

Scott JA, Schumann CM, Goodlin-Jones BL, Amaral DG. A comprehensive volumetric analysis of the cerebellum in children and adolescents with autism spectrum disorder. *Autism Res* 2: 246–257, 2009. doi:10.1002/aur.97.

Sedaghat-Nejad E, Herzfeld DJ, Shadmehr R. Reward prediction error modulates saccade vigor. *J Neurosci* 39: 5010–5017, 2019. doi:10.1523/JNEUROSCI.0432-19.2019.

Shin SL, De Schutter E. Dynamic synchronization of Purkinje cell simple spikes. *J Neurophysiol* 96: 3485–3491, 2006. doi:10.1152/jn.00570.2006.

Siegle JH, López AC, Patel YA, Abramov K, Ohayon S, Voigts J. Open Ephys: an open-source, plugin-based platform for multichannel electrophysiology. *J Neural Eng* 14: 045003, 2017. doi:10.1088/1741-2552/aa5eea.

Smith MA, Ghazizadeh A, Shadmehr R. Interacting adaptive processes with different timescales underlie short-term motor learning. *PLoS Biol* 4: e179, 2006. doi:10.1371/journal.pbio.0040179.

Smith MA, Shadmehr R. Intact ability to learn internal models of arm dynamics in Huntington's disease but not cerebellar degeneration. *J Neurophysiol* 93: 2809–2821, 2005. doi:10.1152/jn.00943.2004.

Soetedjo R, Fuchs AF. Complex spike activity of Purkinje cells in the oculomotor vermis during behavioral adaptation of monkey saccades. *J Neurosci* 26: 7741–7755, 2006. doi:10.1523/JNEUROSCI.4658-05.2006.

Soetedjo R, Kojima Y, Fuchs AF. Complex spike activity in the oculomotor vermis of the cerebellum: a vectorial error signal for saccade motor learning? *J Neurophysiol* 100: 1949–1966, 2008. doi:10.1152/jn.90526.2008.

Solomon SG, Rosa MG. A simpler primate brain: the visual system of the marmoset monkey. *Front Neural Circuits* 8: 96, 2014. doi:10.3389/fncir.2014.00096.

Sugihara I, Marshall SP, Lang EJ. Relationship of complex spike synchrony bands and climbing fiber projection determined by reference to aldolase C compartments in crus IIa of the rat cerebellar cortex. *J Comp Neurol* 501: 13–29, 2007. doi:10.1002/cne.21223.

Takagi M, Zee DS, Tamargo RJ. Effects of lesions of the oculomotor vermis on eye movements in primate: saccades. *J Neurophysiol* 80: 1911–1931, 1998. doi:10.1152/jn.1998.80.4.1911.

Takahashi DY, Liao DA, Ghazanfar AA. Vocal learning via social reinforcement by infant marmoset monkeys. *Curr Biol* 27: 1844–1852.e6, 2017. doi:10.1016/j.cub.2017.05.004.

Tang T, Blenkinsop TA, Lang EJ. Complex spike synchrony dependent modulation of rat deep cerebellar nuclear activity. *eLife* 8: e40101, 2019. doi:10.7554/eLife.40101.

Tang T, Suh CY, Blenkinsop TA, Lang EJ. Synchrony is key: complex spike inhibition of the deep cerebellar nuclei. *Cerebellum* 15: 10–13, 2016. doi:10.1007/s12311-015-0743-z.

Thier P, Dicke PW, Haas R, Barash S. Encoding of movement time by populations of cerebellar Purkinje cells. *Nature* 405: 72–76, 2000. doi:10.1038/35011062.

Wakabayashi M, Koketsu D, Kondo H, Sato S, Ohara K, Polyakova Z, Chiken S, Hatanaka N, Nambu A. Development of stereotaxic recording system for awake marmosets (*Callithrix jacchus*). *Neurosci Res* 135: 37–45, 2018. doi:10.1016/j.neures.2018.01.001.

Wang X. Cortical coding of auditory features. *Annu Rev Neurosci* 41: 527–552, 2018. doi:10.1146/annurev-neuro-072116-031302.

Wang X, Lu T, Snider RK, Liang L. Sustained firing in auditory cortex evoked by preferred stimuli. *Nature* 435: 341–346, 2005. doi:10.1038/nature03565.

Warnaar P, Couto J, Negrello M, Junker M, Smilgin A, Ignashchenkova A, Giugliano M, Thier P, De Schutter E. Duration of Purkinje cell complex spikes increases with their firing frequency. *Front Cell Neurosci* 9: 122, 2015. doi:10.3389/fncel.2015.00122.

Welsh JP, Lang EJ, Suglhara I, Llinás R. Dynamic organization of motor control within the olivocerebellar system. *Nature* 374: 453–457, 1995. doi:10.1038/374453a0.

Whitney ER, Kemper TL, Bauman ML, Rosene DL, Blatt GJ. Cerebellar Purkinje cells are reduced in a subpopulation of autistic brains: a stereological experiment using calbindin-D28k. *Cerebellum* 7: 406–416, 2008. doi:10.1007/s12311-008-0043-y.

Wise AK, Cerminara NL, Marple-Horvat DE, Apps R. Mechanisms of synchronous activity in cerebellar Purkinje cells. *J Physiol* 588: 2373–2390, 2010. doi:10.1113/jphysiol.2010.189704.

Xu-Wilson M, Chen-Harris H, Zee DS, Shadmehr R. Cerebellar contributions to adaptive control of saccades in humans. *J Neurosci* 29: 12930–12939, 2009. doi:10.1523/JNEUROSCI.3115-09.2009.

Yoon T, Geary RB, Ahmed AA, Shadmehr R. Control of movement vigor and decision making during foraging. *Proc Natl Acad Sci USA* 115: E10476–E10485, 2018. [Erratum in *Proc Natl Acad Sci USA* 115: E11884, 2018.] doi:10.1073/pnas.1812979115.